Supporting information to accompany:

Ab Initio-based Determination of Lanthanoid-Radical Exchange as Visualised by Inelastic Neutron Scattering

Maja A. Dunstan, Marcus J. Giansiracusa, Simone Calvello, Lorenzo Sorace, Anwen M. Krause-Heuer, Alessandro Soncini, Richard A. Mole, Colette Boskovic

Contents:

Introduction

Table S1: Compilation of select literature examples of lanthanoid-radical exchange coupled systems.

Ligand based radical	Ln-radical Coupling Strength (cm^{-1})	Coupling method	Ref
[GdTp$_2$dbsq]	-5.7	S-only	[1]
[Gd(hfac)$_3$(2pyNO)]	-11	S-only	[2]
[Dy(hfac)$_3$(2pyNO)]	-39.9	J_z-S_z	[3]
[((Me$_3$Si)$_2$N]$_2$(THF)Gd)$_2$(μ-N$_2$)]	-27	S-only	[4]
[((Me$_3$Si)$_2$N]$_2$(THF)Tb)$_2$(μ-N$_2$)]	-20.2	J-S - B20 only	[4]
[((Me$_3$Si)$_2$N]$_2$(THF)Dy)$_2$(μ-N$_2$)]	-7.3	J-S - B20 only	[4]
[(Cp^{Me4H})$_2$Gd$_2$(μ-N$_2$)]	-20	S-only	[4]
[(Cp^{Me4H})$_2$Tb$_2$(μ-N$_2$)]	-23.1	J-S - B20 only	[4]
[(Cp^{Me4H})$_2$Dy$_2$(μ-N$_2$)]	-7.2	J-S - B20 only	[4]
[Gd$_2$(μ-BzN$_6$-Mes)]	-43	S-only	[5]
[(Cp*$_2$Gd)$_2$(pyz$^{•-}$)(THF)$_2$](BPh$_4$)	-22	S-only	[6]
[(Cp*$_2$Gd)$_2$(tz$^{•-}$)(THF)$_2$](BPh$_4$)	−7.2	S-only	[7]
[(Cp*$_2$Gd)$_2$(μ-η^2:η^2-Bi$_2$$^•$)]	−15.9(2)	S-only	[8]
[(Cp*$_2$Tb)$_2$(μ-η^2:η^2-Bi$_2$$^•$)]:	-19		[8]
[(Cp*$_2$Dy)$_2$(μ-η^2:η^2-Bi$_2$$^•$)]:	-24		[8]
Localised radical centre	Ln-radical Coupling Strength (cm^{-1})	Blocking Temperature (T_B)	Ref
[Gd$_2$@C$_{79}$N]	170(10)	S-only	[9,10]
[Gd$_2$@C$_{80}$(CH$_2$Ph)]	160(10)	S-only	[9,10]
[Tb$_2$@C$_{80}$(CH$_2$Ph)]	-45		[7]
Gd$_2$I$_3$Cp$_2$	387(4)	S-only	[11]

Experimental Section

Synthesis

The synthesis of **Er-dbsq**, **Er-dbsq^D**, and **Y-dbsq** was performed using standard Schlenk techniques under an atmosphere of dry nitrogen before exposure to ambient atmosphere. All other syntheses and manipulations were undertaken under ambient atmosphere. All chemicals purchased were of reagent grade or higher and used as received. The ligand KTp was synthesised according to a modified literature procedure.[12]

3,5-di-tert-butyl-1,2-catechol-d$_{20}$ (dbcatH$_2$-d$_{20}$): 3,5-di-tert-butylcatechol (Sigma) (10 g, 45.0 mmol), Pt/C (10%, 1.0 g, 0.5 mmol), Pd/C (10%, 1.0 g, 0.9 mmol) and D$_2$O (150 mL, 7.5 mol) were placed in a Parr pressure reactor (450 mL capacity) and the vessel purged by bubbling through with a flow of N$_{2(g)}$ and then H$_{2(g)}$. The reactor was sealed and heated to 180°C with stirring for 16 h.

The reaction contents were filtered through a short plug of celatom filter aid, and the reactor washed with CH$_2$Cl$_2$ to dissolve the thick tarry substance that had formed, with the celatom then washed with further CH$_2$Cl$_2$ until the filtrate was mostly colourless. The dark green organics were dried over Mg$_2$SO$_4$ and concentrated to give a dark green, thick oil. The crude product was purified in batches on silica used automated medium pressure chromatography (Buchi Reveleris), eluting with 100% CH$_2$Cl$_2$. The fractions containing the product were identified on thin layer chromatography (100% CH$_2$Cl$_2$, visualised with Hanessian's dip), combined and evaporated to give a brown solid (5.0 g, 46% yield), with an overall average deuteration level of 89% as calculated by mass spectrometry. ^{1}H NMR (400 MHz, CDCl$_3$): 6.87 (br, residual H), 6.75 (br, residual H), 5.42 (br, OH), 1.38 (m, residual CH$_3$), 1.23 (m, residual CH$_3$). ^{2}H NMR (60 MHz, CDCl$_3$): 6.93, 6.80, 1.39, 1.25. ^{13}C NMR (101 MHz, CDCl$_3$): 142.4 (s), 142.3 (s), 140.8 (s), 135.8 (s), 115.9 (m), 110.3 (m), 34.4 (m), 33.8 (m), 30.9 (m), 29.0 (m). ^{13}C NMR {^{1}H, ^{2}H decoupled}: 142.2 (s), 142.1 (s), 140.7 (s), 135.7 (s), 115.8 (s),

110.1 (s), 34.2 (m), 33.6 (m), 30.8 (m), 28.9 (m). EMS MS⁻: [M-H]⁻ calculated $[C_{14}HD_{20}O_2]^-$ 241.3, found 241.3. Isotopic distribution d_{10} 0.2%, d_{11} 0.2%, d_{12} 0.4%, d_{13} 0.6%, d_{14} 2.0%, d_{15} 3.6%, d_{16} 6.5%, d_{17} 12.1%, d_{18} 21.5%, d_{19} 25.0%, d_{20} 17.6%. Overall calculated percentage deuteration 89%.

Potassium hydro-tris(1-pyrazolyl)borate (KTp): The synthesis of KTp was adapted from Trofimenko.[12] A mixture of pyrazole (25.0 g, 275.7 mmol) and potassium borohydride (4.96 g, 91.9 mmol) was slowly heated to melting (120 °C) and stirred for an hour. The temperature was raised gradually to 180 °C and heated with stirring for 24 hours. Sublimed reagent and products were occasionally knocked back into the reaction mixture. The melt was then cooled to ~110 °C, and boiling toluene added, causing precipitation of a white solid. The solid was collected by hot filtration, and washed with copious hot toluene, yielding a pure-white solid, 19.1 g, 82%. The obtained solid was pure by ^{1}H NMR and used without further purification. ^{1}H NMR (D_2O, ppm): . Selected FT-IR data (KBr, cm^{-1}): 3609 (m), 3136 (m), 3120 (m), 3092 (w), v_{ArH} 2919 (w), v_{ArH} 2851 (w), v_{BH} 2425 (w), v_{BH} 2399 (w), v_{BH} 2390 (w), v_{BH} 2366 (w), 1640 (w), 1500 (m), 1415 (m), 1386 (s), 1295 (s), 1289 (s), 1215 (s), 1201 (m), 1185 (m), 1125 (s), 1112 (s), 1084 (w), 1071 (w), 1058 (m), 1048 (s), 966 (m), 792 (m), 776 (s), 756 (s), 737 (s), 723 (s), 626 (m).

[ErTp₂trop] (Er-trop): The synthesis was adapted from literature.[13] A suspension of $Er(NO_3)_3 \cdot 5H_2O$ (176 mg, 0.400 mmol) and KTp (210 mg, 0.830 mmol) in methanol (20 mL) was refluxed for 30 minutes, at which time dissolution of most solid had occurred. A solution of tropH (48.8 mg, 0.400 mmol) with one equivalent of Et_3N (56 μL, 0.400 mmol) in methanol (10 mL) was added, and the resulting solution refluxed a further 30 minutes. The reaction mixture was then cooled, and the volume doubled by addition of water. The resulting fine suspension was extracted into dichloromethane (3 × 20 mL), washed with brine (20 mL), dried with MgSO₄, and filtered. The solvent was removed, and the crude solid redissolved in hot

methanol (~20 mL) and filtered. Ethyl acetate (~ 5 mL) was then added to the filtrate, and the solution reduced until the first signs of a crystalline solid appeared. The solution was kept at –18 °C to crystallise overnight. The resulting crystalline solid was collected by vacuum filtration, washed with minimal chilled methanol, and air dried (11.8 mg, 5%) Analysis calculated for $H_{25}B_2C_{25}N_{12}O_2Er$: C, 42.03; H, 3.53; N, 23.53. Found: C: 42.26, H: 3.64, N: 23.58. Selected FT-IR data for **Er-trop** (KBr disk, cm^{-1}): v_{ArH} 2924 (w), v_{BH} 2465 (w), 1591 (m), 1512 (s), 1433 (s), 1404 (m), 1386 (m), 1367 (w), 1299 (m), 1215 (m), 1120 (m), 1053 (s), 975 (w), 767 (m), 723 (m), 671 (w), 625 (w), 511 (w).

[YTp₂trop] (Y-trop): A sample of **Y-trop** was synthesised in the analogous manner to **Er-trop**, for single crystal X-ray diffraction measurements and synthesis of **Er@Y-trop**. A yellow crystalline solid was obtained from recrystallisation in methanol.

[Er₀.₀₅Y₀.₉₅Tp₂trop] (Er@Y-trop): A sample of **Er-trop** diluted in the Y(III) diamagnetic analogue was obtained by first synthesising crude samples of **Er-trop** and **Y-trop**, where **Y-trop** was obtained in the analogous manner to **Er-trop** using $Y(NO_3)_3.6H_2O$ as the rare earth salt. ICP-OES analysis for **Er@Y-trop**: Er 5.20%, Y 94.80%.

[ErTp₂dbsq] (Er-dbsq): The synthesis was adapted slightly from literature.[13] A degassed solution of dbcatH₂ (88.4 mg, 0.100 mmol) in methanol (6 mL) was added with stirring to a degassed suspension of KTp (200 mg, 0.80 mmol) and $Er(NO_3)_3.5H_2O$ (176 mg, 0.39 mmol) in methanol (12 mL). Solid KOH (22.4 mg, 0.40 mmol) was added, and the solution heated to reflux. After reaction for 30 minutes, the solution was exposed to air, the volume doubled by addition of water, and stirred for 30 minutes. The solution was extracted with *n*-hexane (3 × 30 mL), washed with water, dried on MgSO₄, and filtered. The resultant dark blue solution was reduced under vacuum and kept at –18 °C to crystallise. The product was collected by vacuum filtration, washed with chilled *n*-hexane, and air dried, yielding **Er-dbsq** as a dark blue crystalline solid (80 mg, 25%). Selected FT-IR data for **Er-dbsq** (KBr disc, cm^{-1}): v_{CH3} 2962

(m), v_{ArH} 2928 (w), v_{CH3} 2906 (w), v_{CH3} 2870 (w), v_{BH} 2453 (w), 1583 (w), 1533 (m), 1502 (s), 1493 (s), 1406 (s), 1389 (m), 1301 (s), 1215 (s), 1200 (m), 1121 (s), 1065 (m), 1049 (s), 976 (m), 756 (s), 723 (s), 673 (w), 621 (w), 459 (w). Anal. Calcd for $H_{40}B_2C_{32}N_{12}O_2Er$: C, 47.24; H, 4.96; N, 20.66. Found: C, 46.94; H, 5.04; N, 20.40.

[ErTp2d20-dbsq] (Er-dbsq^D): Er-dbsq^D was synthesised in the same manner as **Er-dbsq**, at 5 times scale. The product was recrystallised from *n*-hexane to obtain a dark blue crystalline product (408 mg, 25%). The synthesis was repeated multiple times and combined for INS measurements. Selected FT-IR data (KBr disc, cm^{-1}): v_{CH3} 2961 (w), v_{ArH} 2930 (w), v_{CH3} 2455 (w), v_{CD3} 2216 (w), v_{CD3} 2131 (w), v_{CD3} 2071 (w), 1524 (m), 1504 (m), 1483 (s), 1460 (m), 1406 (s), 1389 (m), 1302 (s), 1215 (s), 1121 (s), 1065 (m), 1047 (s), 976 (m), 781 (w), 756 (s), 735 (m), 723 (s), 673 (w), 621 (w), 457 (w).

[YTp2d20-dbsq] (Y-dbsq^D): Y-dbsq^D was synthesised following the procedure of **Er-dbsq^D**, using Y(NO$_3$)$_3$.6H$_2$O as the rare earth salt, yielding dark blue crystalline product (445 mg, 24%). The synthesis was repeated multiple times and combined for INS measurements.

Compounds **Er-trop** and **Y-trop** were synthesised according to a modified literature procedure.[13] The doped sample **Er@Y-trop** was obtained by combining crude **Y-trop** and **Er-trop** in a Y:Er ratio of 19:1, followed by recrystallisation from methanol/ethyl acetate. The hydrogenous **Er-dbsq** was synthesised following the published procedure.[13] To lower the hydrogenous background, and to remove some of the QENS signal due to *tert*-butyl group rotation at low energy, where we expect to observe exchange transitions in the INS spectrum, we deuterated the proligand dbcatH$_2$. The dbcatH$_2$-d$_{20}$ was synthesised from the hydrogenous compound, by hydrothermal H/D exchange with D$_2$O with catalytic Pd/C and Pt/C in a Parr reactor. An overall deuteration of 89% (excluding the hydroxyl protons) for the dbcatH$_2$-d$_{20}$ was determined from ^{1}H/^{2}H NMR spectroscopy and ESI-MS. Deuterated analogues **Y-dbsq^D** and **Er-dbsq^D** for inelastic neutron scattering measurements were obtained in an analogous

manner to **Y-dbsq** and **Er-dbsq**, using 3,5-dbcatH$_2$-d$_{20}$, at four times the scale – subsequent batches were then combined for measurement. Additional discussion of the synthesis and characterization of the compounds by IR spectroscopy, NMR spectroscopy, powder X-ray diffraction, and powder neutron diffraction are outlined in the Supporting Information.

X-ray diffraction and structure solution

X-ray diffraction patterns were obtained on an XtaLAB Synergy-S diffractometer from Rigaku Oxford Diffraction with a HyPix-6000HE detector, using Cu-K$_\alpha$ (λ = 1.5406 Å) radiation. All X-ray diffraction data were collected at 100 K.

Tetragonal pale yellow block crystals of **Y-trop** were grown from a concentrated solution in methanol at –18 °C. Yellow block crystals of **Er@Y-trop** and pale pink block crystals of **Er-trop** were obtained in the same manner. Dark blue rhombohedral block crystals of **Er-dbsq** suitable for single crystal X-ray diffraction were grown from a concentrated reaction solution in *n*-hexane at –18 °C. Crystals for all samples were transferred directly from solution to crystallographic oil. The data were reduced using CrysalisPro[14] using a numerical absorption correction based on Gaussian integration over a multi-faceted crystal model. The structures were solved using the SHELXT structure solution program[15] using Intrinsic Phasing and refined with the SHELXL refinement package[16] using Least Squares minimization on F^2 on all data, in the graphical user interface OLEX2.[17] All non-hydrogen atoms were refined using anisotropic displacement parameters, while hydrogen atoms were placed at geometrical estimates and refined using the riding model.

The compounds **Y-trop**, **Er-trop,** and **Er@Y-trop** are all isostructural and isomorphous, with slight differences in cell parameters due to the difference in ionic radius between Y(III) and Er(III). The rare earth center in compound **Er@Y-trop** was solved in two parts, with the occupancy of the Er and Y allowed to refine freely, with the sum of occupancies fixed to 1. The rare earth ions were refined to have the same position and equivalent atomic displacement

parameters. This was performed on three separate crystals, where in each case, the relative occupancies of Er:Y refined to ratios between 4:96 and 5:95, consistent with ICP-OES results. This demonstrated that the doping was consistent within each crystallite and the sample isn't a mix of crystallites of **Er-trop** and crystallites of **Y-trop**.

X-ray powder diffraction patterns were collected by loading a lightly crushed sample into a 3 mm borosilicate glass capillary for measurement and data were collected using a Gandolfi move for powder samples, to $2\theta = 70°$ with an exposure time of 60 seconds. X-ray powder diffraction patterns were simulated from the single crystal X-ray structures in Mercury.[18]

Magnetic measurements

Magnetic measurements were performed on a Quantum Design Physical Properties Measurement System (PPMS) with an AC Measurement System (ACMS) insert. Static (dc) magnetic susceptibility measurements were measured in an applied dc field of 0.1 T. Ferromagnetic checks were performed on all samples, to confirm the absence of paramagnetic impurities. The powder samples were prepared in gelatine capsules, and **Er-trop** and **Er-dbsq** were restrained in eicosane wax to prevent magnetic torquing. Static magnetic susceptibility and magnetisation measurements were corrected for the eicosane and gel cap contributions and corrected for the diamagnetic component of the sample using Pascal's constants.

Electron paramagnetic resonance

Electron paramagnetic resonance measurements for microcrystalline powder of **Er-trop** and **Er@Y-trop** were obtained at 5 K on a Bruker E500 spectrometer equipped with an ESR900 (Oxford Instruments) continuous flow ^{4}He cryostat and a SHQ resonator.

The EPR spectra at 5 K for **Er-trop** and **Er@Y-trop** were simulated using the function pepper in the software Easyspin[19] employing the *ab initio* calculated effective *g*-values of the ground doublet as input, with line-width broadening, A_{eff}, hyperfine tensor and *g*-strain as discussed in the results.

Neutron scattering

Inelastic neutron scattering experiments were performed using the Pelican cold neutron time-of-flight spectrometer[20,21] at the Australian Centre for Neutron Scattering. Powder samples of 1.5 – 2 g of the partially deuterated **Y-dbsq^D** and **Er-dbsq^D** were placed in an annular aluminium can with a 0.5 mm gap, chosen to give a 10% scatter and minimise multiple scattering events. The sample can was mounted in an Oxford Instruments CCR type cryostat with a secondary cooling circuit, with ~30 mbar of He exchange gas. Both samples were measured with λ = 4.69 Å (affording a higher resolution of 0.135 meV at the elastic line) and $\lambda/2$ = 2.34 Å (affording a resolution of 0.80 meV at the elastic line) neutrons. The $\lambda/2$ configuration allows a broader energy transfer range on the energy loss-side of the spectrum, despite the loss in resolution. Unless otherwise noted, all samples were measured for 4 hours at $\lambda/2$, and 8 hours at λ wavelengths.

The background due to the empty sample can was subtracted for the spectra used for analysis of the powder neutron diffraction and phonon generalised density of states, and the **Y-dbsq^D** spectra, normalised by number of moles of sample, was subtracted as a pseudo-diamagnetic background for analysis of magnetic excitations. The data were all normalised to a vanadium standard, to correct for detector efficiencies. Data were then converted to $S(\boldsymbol{Q},\omega)$. A constant $\boldsymbol{Q}$-range was used across the energy range analysed for comparison of magnetic peak intensities. All manipulations on the data were carried out using the Large Array Manipulation Program (LAMP).[22]

Spectra were simulated from electronic structure calculations and the wavefunctions simulated through PHI[23] using the Lines model by calculation of a relative transition probability for each transition by Boltzmann population of the initial state and transition probability between states. Gaussians were then plotted using the relative transition

probabilities with the FWHM from instrument resolution at that energy transfer and wavelength (chosen to match the experimental data).

Other measurements

Fourier transform infrared (FT-IR) spectra were measured as KBr discs on a Bruker Tensor 27 FTIR spectrometer and normalised as absorbance spectra. The ^{1}H NMR spectrum of KTp was acquired on a Varian MR400 400 MHz spectrometer and referenced to residual protic solvent.

Elemental analyses (CHN) were performed at the Campbell Microanalytical Laboratory, University of Otago. Inductively Coupled Plasma – Optical Emission Spectroscopy (ICP-OES) was measured on a Perkin Elmer Optima 4300 DV spectrometer, with the Y concentration determined by integration of peaks at $\lambda = 360.073$ nm and 324.227 nm, and the Er concentration determined at $\lambda = 337.271$ nm and 349.910 nm.

Computational details

Wavefunction based electronic structure calculations were performed on the atomic coordinates of **Er-trop** and **Er-dbsq**, as obtained from single-crystal X-ray diffraction, to support the analysis of both magnetic (*i.e.* magnetic susceptibility, and magnetization) and exchange coupling properties. All calculations have been performed on NeCTAR research cloud virtual machines, and feature State-Averaged Complete Active Space Self-Consistent Field (SA-CASSCF)[24] optimizations, one for each spin manifold, coupled to the Restricted Active Space State Interaction with Spin-Orbit (RASSI-SO) method,[25] as implemented in the quantum chemistry package OPENMOLCAS.[26,27]

Relativistic effects, which are of paramount importance to correctly describe the electronic and magnetic features of the lanthanoid ion, are introduced in the CASSCF/RASSI-SO method in two steps. First, scalar relativistic terms are included through both the use of basis sets optimised for relativistic calculations (ANO-RCC)[28] and the inclusion of relativistic

contributions within the second order Douglas–Kroll–Hess (DKH2) approximation,[29] in the one-electron part of the electrostatic Hamiltonian which is used to optimise the SA-CASSCF wave functions. Afterwards, an effective one-electron spin-orbit coupling Hamiltonian, where average two-electron contributions are accounted for through the Atomic Mean Field Interaction (AMFI) approximation,[29] is diagonalised in the basis of all optimised SA-CASSCF spin states within the RASSI-SO method. The magnetic properties and m_J compositions of the resulting wave functions are then obtained using the SINGLE-ANISO routine.[30]

The basis set employed to describe atoms in **Er-trop** calculations is ANO-RCC[28] with contractions of, respectively, [8s7p5d3f2g1h] for Er, [3s2p1d] for coordinating O and N, [3s2p] for non-coordinating O, N, and C and B and [2s] for H. For **Er-dbsq**, the C and O atoms of the semiquinone right were increased to [4s3p2d1f]. In order to speed up the calculation of the two-electron atomic integrals, Cholesky decomposition[31] has been employed, with a cut-off threshold of $\delta = 10^{-8}$.

The active space for the **Er-trop** calculation is composed of the seven $4f$ orbitals of the Er(III) ion occupied by its 11 electrons. In separate SA-CASSCF calculations, the 35 $s = 3/2$ and 112 $s = 1/2$ states have been optimised, and subsequently mixed via spin-orbit coupling. In the case of the **Er-dbsq** calculation, the active space is composed of the seven $4f$ orbitals of the Er(III) ion, occupied by its 11 electrons, and the singly occupied, delocalised π orbital of the dbsq− ligand.

The spin state selection for the exchange coupled system was determined through sequential testing of the orbital description with increasing spin state terms in the SA-RASSCF step. For each iteration, the average orbital occupation was examined to ensure chemically logical localization of the non-bonding $4f$ orbitals. The chosen number of spin states included in the final calculation include 30 quintets and 32 triplets, with no singlet states. These numbers arise from the 4 lowest lying spin terms for each spin state. These originate from ferromagnetic

coupling with the Er(III) spin terms ^{4}I, ^{4}F, ^{4}S and ^{4}G for the quintets and a mixture of ferro and antiferromagnetic coupling with the Er(III) spin terms ^{4}I, ^{2}H, ^{4}F and ^{4}S for the triplet. All optimised roots were mixed in the RASSI spin-orbit coupling method and the magnetic properties and effective *g*-tensor terms were calculated using Single_Aniso. The spin states calculated by the RASSCF indicate the lowest lying state is a triplet, arising from antiferromagnetic coupling between the Er(III) and radical.

Effective g-values are often assigned for non-Kramers ions where states are non-degenerate, so in a similar way using Single_Aniso in Molcas, the effective g-values of a pseudo doublet are calculated. Antiferromagnetic coupling an isotropic spin with the highly anisotropic ground doublet state of Er would lead to lowering the effective magnetic moment of the exchange ground state (while raising the ferromagnetic excited state). Taking an Ising-like exchange as example, the doublet would split into two degenerate doublet states of $\langle\Uparrow\downarrow\rangle$, $\langle\Downarrow\uparrow\rangle$ and $\langle\Uparrow\uparrow\rangle$, $\langle\Downarrow\downarrow\rangle$. In this picture, the g-values of the states following the Ising exchange would be ±2 on g_z, centred at the g_z value of the crystal field state of the Er ion. For ground state with $g_z = 14.7$ (*vide infra*), an Ising like antiferromagnetic exchange would lead to ground doublet with $g_z \approx 12.7$ and an excited doublet with $g_z \approx 16.7$

Powder diffraction and crystallography

To confirm the phase purity of the bulk samples, powder X-ray diffraction was measured for all samples, and compared to the pattern simulated from the single-crystal X-ray data for the Er analogues (SI Figures S1-3). There is excellent agreement between the simulated and experimental patterns for all compounds, confirming phase purity. Additionally, an INS experiment on a time-of-flight instrument allows simultaneous collection of a powder neutron diffraction (PND) pattern. Powder neutron diffraction patterns were simulated in FullProf[32], using the unit cell and atomic coordinates obtained from single crystal X-ray diffraction of **Er-dbsq**, with the ^{1}H atoms on the dbsq$^{\bullet-}$ changed to ^{2}H atoms in the input file, to account for the different neutron scattering lengths of the two isotopes. The PND patterns of **Y-dbsq^D** and **Er-dbsq^D** are identical, and match the simulated diffraction peaks well, confirming that no phase changes occur at low temperature.

Table S2. Crystallographic data for compounds **Er-trop** and **Er-dbsq**.

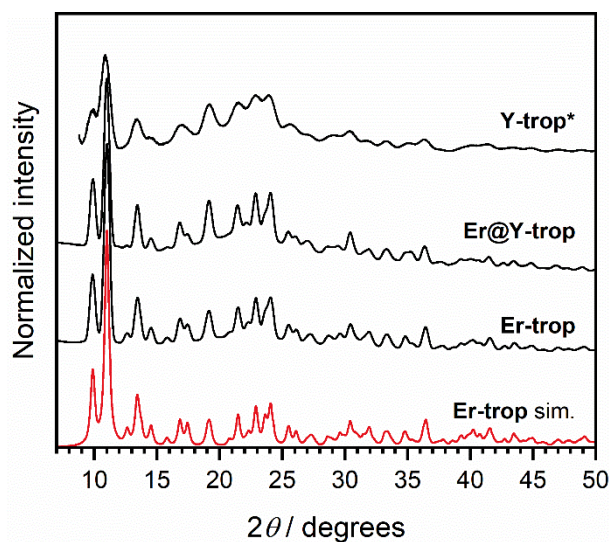|	Er-trop	Er-dbsq	Y-trop	Er@Y-trop
Empirical formula	$C_{25}H_{25}B_2N_{12}O_2Er$	$C_{32}H_{40}B_2N_{12}O_2Er$	$C_{25}H_{25}B_2N_{12}O_2Y$	$C_{25}H_{25}B_2Er_{0.04}N_{12}O_2Y_{0.96}$
Formula weight	714.45	813.64	636.1	639.23
Temperature/K	100.00(10)	99.99(10)	100.0(3)	100.00(10)
Crystal system	Tetragonal	Monoclinic	Tetragonal	Tetragonal
Space group	$P4_12_12$ ($P4_32_12$)	$P2_1/c$	$P4_12_12$ ($P4_32_12$)	$P4_32_12$ ($P4_12_12$)
a/Å	9.32610(10)	12.59650(10)	9.33650(10)	9.33390(10)
b/Å	9.32610(10)	14.87660(10)	9.33650(10)	9.33390(10)
c/Å	31.8683(5)	19.51760(10)	31.9312(7)	31.9618(6)
β/°	90	98.3210(10)	90	90
V/Å^3	2771.78(7)	3618.96(4)	2783.45(9)	2784.57(8)
Z	4	4	4	4
ρ_{calc}/gcm^{-3}	1.712	1.493	1.518	1.525
μ/mm^{-1}	6.022	4.683	3.353	3.457
$F(000)$	1412	1640	1296	1301
Crystal size/mm^3	0.25 × 0.153 × 0.093	0.133 × 0.079 × 0.038	0.123 × 0.076 × 0.05	0.117 × 0.072 × 0.046
Radiation	CuKα (λ = 1.54184)	CuKα (λ = 1.54184)	Cu Kα (λ = 1.54184)	Cu Kα (λ = 1.54184)
2Θ range/°	9.882 to 152.986	7.092 to 156.148	9.87 to 152.776	9.872 to 153.398
Index ranges	$-11 \leq h \leq 9$, $-9 \leq k \leq 11$, $-26 \leq l \leq 40$	$-15 \leq h \leq 15$, $-18 \leq k \leq 18$, $-17 \leq l \leq 24$	$-7 \leq h \leq 11$, $-11 \leq k \leq 5$, $-37 \leq l \leq 40$	$-11 \leq h \leq 6$, $-7 \leq k \leq 11$, $-39 \leq l \leq 28$
Reflections collected	9357	54321	9108	9327
Independent reflections	2822 [R_{int} = 0.0407, R_{sigma} = 0.0369]	7666 [R_{int} = 0.0342, R_{sigma} = 0.0205]	2827 [R_{int} = 0.0470, R_{sigma} = 0.0466]	2772 [R_{int} = 0.0381, R_{sigma} = 0.0350]
Data/restraints/parameters	2822/0/191	7666/0/448	2827/0/191	2772/0/192
Goodness-of-fit on F^2	1.071	1.069	1.064	1.077
Final R indexes [$I \geq 2\sigma(I)$]	R_1 = 0.0277, wR_2 = 0.0694	R_1 = 0.0262, wR_2 = 0.0684	R_1 = 0.0301, wR_2 = 0.0737	R_1 = 0.0258, wR_2 = 0.0666
Final R indexes [all data]	R_1 = 0.0289, wR_2 = 0.0702	R_1 = 0.0270, wR_2 = 0.0689	R_1 = 0.0324, wR_2 = 0.0747	R_1 = 0.0271, wR_2 = 0.0672
Largest diff. peak/hole / e Å^{-3}	0.57/−0.82	0.82/−0.95	0.43/−0.59	0.44/−0.44
Flack parameter	−0.025(10)	—	0.002(11)	−0.037(8)

Figure S1. X-ray powder diffraction patterns of **Y-trop**, **Er-trop**, and **Er@Y-trop**, with simulated pattern from the single crystal X-ray data of **Er-trop**. **Y-trop** was collected with Mo Kα radiation and converted to the equivalent values in 2θ for Cu Kα.
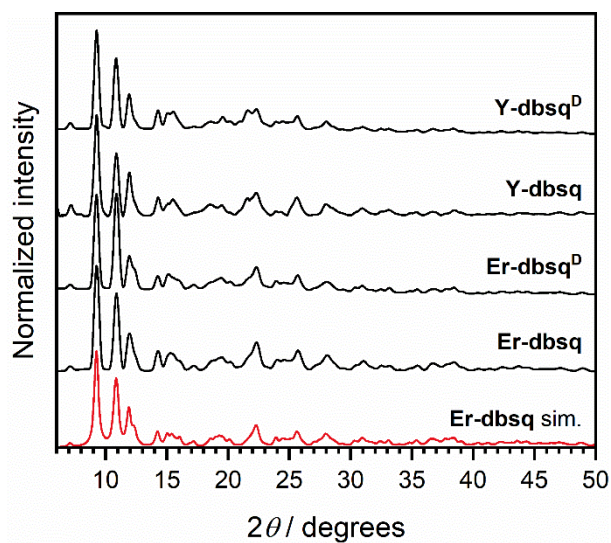

Figure S2. X-ray powder diffraction patterns of **Y-dbsq**, **Y-dbsq^D**, **Er-dbsq,** and **Er-dbsq^D**, with simulated pattern from the single crystal X-ray data of **Er-dbsq** collected with Cu Kα radiation.
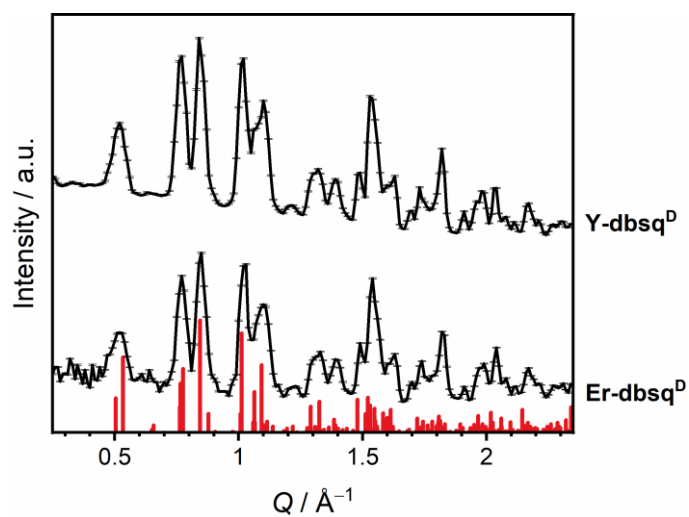
Figure S3. Neutron powder diffraction patterns of **Y-dbsq^D** and **Er-dbsq^D** (black curves) with simulated neutron diffraction pattern assuming a fully deuterated **dbsq$^{\bullet-}$** ligand.
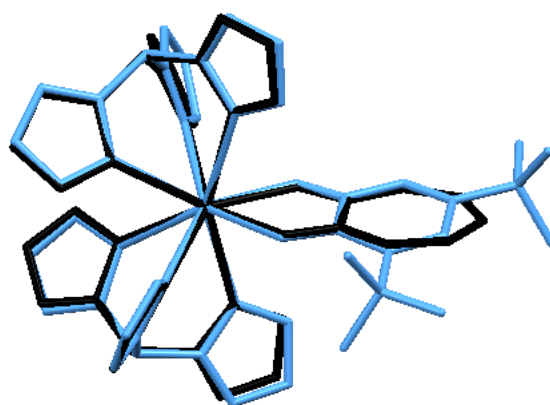
Figure S4. Overlay diagram of **Er-trop** (black) and **Er-dbsq** (light blue) with a root mean square difference of 0.0724 calculated over the coordinating atoms.

Infrared spectroscopy

Infrared spectroscopy was used to confirm the structure of synthesised compounds. The IR spectra of **Y-trop**, **Er@Y-trop**, and **Er-trop** are identical as expected as they are isostructural; with a notable stretch at $v = 2400$ cm^{-1}, attributable to the B-H stretch of the bound Tp$^-$ ligand (Figure S5). The IR spectra of **Y-dbsq** and **Er-dbsq** are again identical with each other, also featuring the characteristic B-H stretch (SI Figure S6). Notably, there is a large C-H stretch at $v = 3000$ cm^{-1} attributable to *t*-Bu groups of the dbsq$^{\bullet-}$ ligand. The IR spectra of the two deuterated analogues again overlay (Figure S7). There are distinct differences between the hydrogenous **Ln-dbsq** and **Ln-dbsq^D** analogues, which correspond to the differences between the hydrogenous and deuterated dbsq$^{\bullet-}$ ligand – the intensity of the bands in the region $v = 300$ cm^{-1} decrease significantly, with significant intensity now at $v = 2,000$ cm^{-1}, consistent with a C-D stretch, confirming significant deuteration.
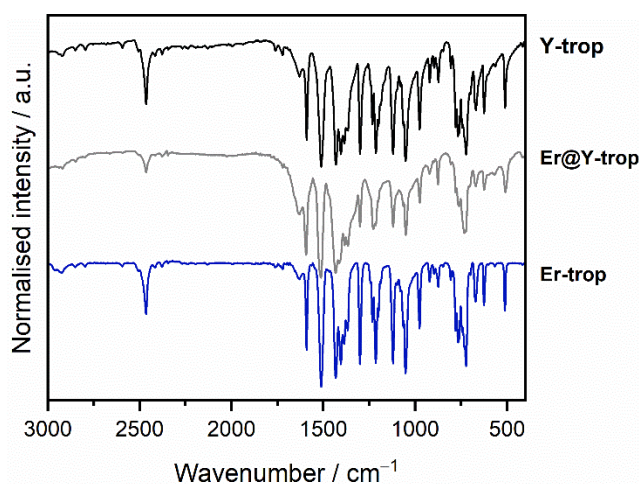
Figure S5. Infrared spectra (KBr disk) of **Y-trop** (upper, black), **Er@Y-trop** (red), **Er-trop** (lower, blue).
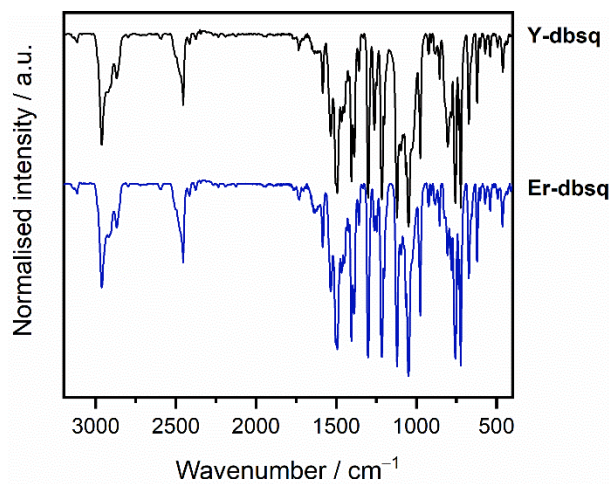
Figure S6. Infrared spectra (KBr disk) of **Y-dbsq** (upper, black) and **Er-dbsq** (lower, blue).
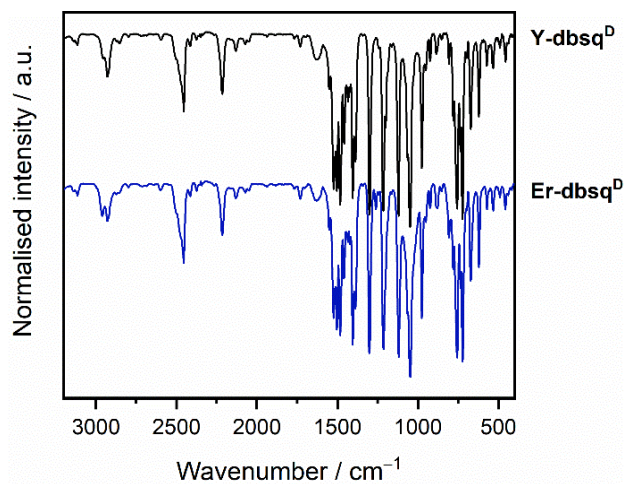

Figure S7. Infrared spectra (KBr disk) of deuterated analogues **Y-dbsq^D** (upper, black) and **Er-dbsq^D** (lower, blue).

EPR spectroscopy

The best simulation of the experimental data for **Er@Y-trop** from the fitted g-tensors ($g_x = 0.01$, $g_y = 0.82$, $g_z = 14.0$) was obtained by inclusion of a Gaussian line width of of 3 mT, and a H-strain on g_y of 700 MHz.
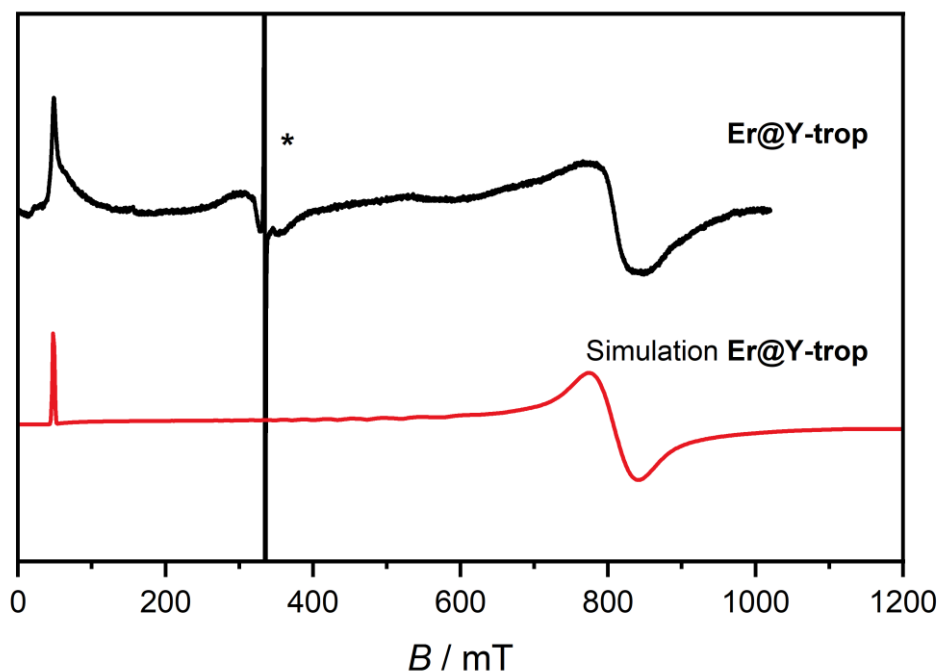

Figure S8. Solid state X-band EPR spectra measured at 5 K for **Er@Y-trop** (black, top) with simulated spectra as described in the text (red, bottom). An asterisk marks the location of a paramagnetic $g = 2.00$ impurity.

Static magnetic measurements
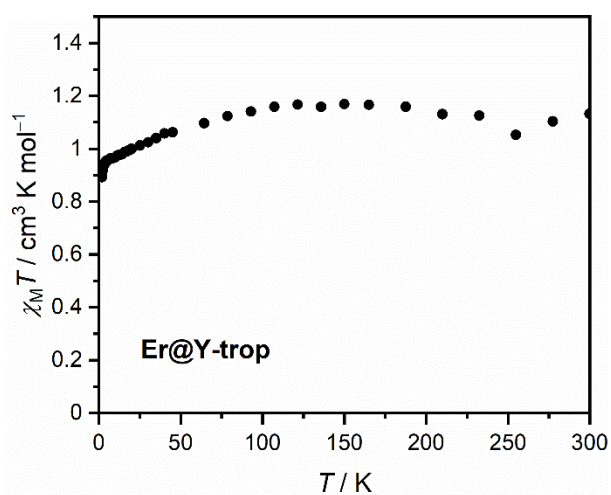
Figure S9. Static magnetic susceptibility data for **Er@Y-trop** measured with $B_{dc} = 0.1$ T (black dots).
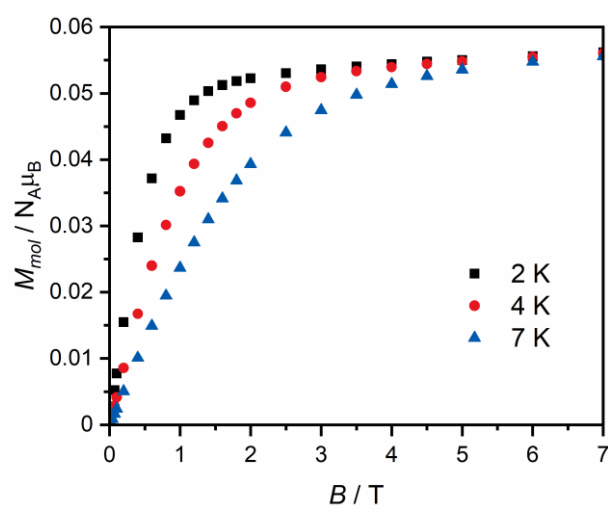
Figure S10. Magnetization data for **Er@Y-trop** measured at 2 K (black squares), 4 K (red circles), and 7 K (blue triangles).

Inelastic neutron scattering

The generalised phonon density of states provides additional evidence of the nature of the four observed features in the INS spectrum of **Er-dbsq^D**. The generalised phonon density of states, $g(\omega)$, is calculated using:

$$g(\omega) = \frac{\omega}{Q^2} S(Q, \omega)(1 - e^{-(\frac{\hbar\omega}{kT})}) \qquad (S1)$$

Where Q is the wavevector transfer and $S(Q, \omega)$ is the scattering function in Q and energy dimensions. A temperature corrected GDOS will correct the intensity of the phonon spectra by their Bose-Einstein populations and should overlay with varying temperature for harmonic phonons. In the temperature dependent $g(\omega)$ in Figure S11 is evident that the region at $E = 5.5$ meV obeys Bose-Einstein statistics, as is expected of a phonon, while the three transitions **a**, **I**, and **II** do not, consistent with CF or magnetic exchange transitions.
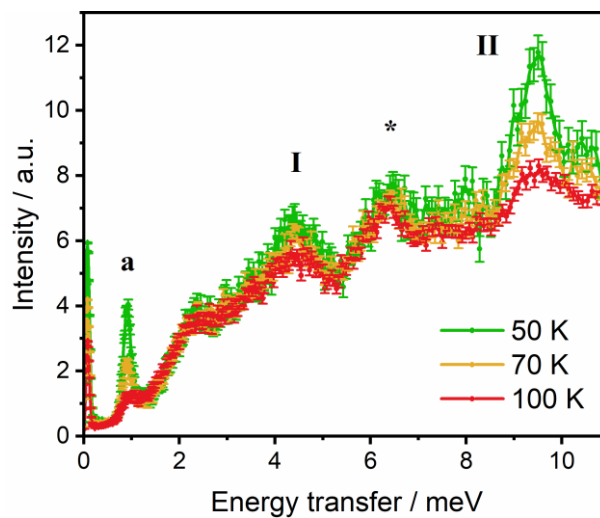

Figure S11. $g(\omega)$ calculated for **Er-dbsq^D** with varying temperature, with CF transitions marked **I** and **II**, and exchange transition marked **a**.

Analysis of the Q-dependence gives spatial information about a transition. The Q-dependence of **I** and **II** at low Q and low temperature show a decrease in intensity with increasing Q, particularly at low Q in the measured range consistent with a CF transition (SI Figures 15, 16, 17). A CF transition should follow a $F^2(Q)$ dependence, where we use the dipole approximation of the magnetic form factor of Er(III).[33] At higher Q there is a deviation from the form factor fall off $F^2(Q)$ behaviour which describes a CF transition, perhaps due to weak

phonons in these regions of the spectra. However, the intensity at low Q is inconsistent with a phonon transition, and this and their temperature dependence allows us to assign them as CF transitions.

The Q-dependence of transition **a** is not conclusive. It follows a reasonable agreement with the $F^2(Q)$ dependence of Er(III) (Figure S12).
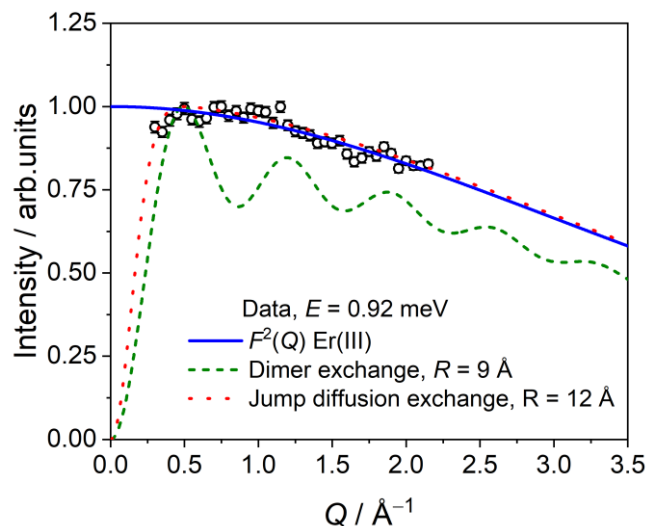

Figure S12. Q-dependence of the transition with $\Delta E = 0.918$ meV (exchange transition marked **a**) compared to predicted Q-dependence for $F^2(Q)$ of Er(III) (blue), dimer exchange (green dash) or a jump diffusion-like model (red dash). See below for additional details.

We then attempted to model the exchange using a metal dimer exchange model (Equation S2):[34]

$$I(Q) \propto F^2(Q)(1 - \frac{sin(QR)}{QR}) \qquad (S2)$$

Using the dimer exchange model, a distance between interacting centres of ~9 Å is obtained, significantly larger than the ~3 Å Er···SQ distance. A jump diffusion-like model, as described by Gransbury *et al.* was also used,[35] however, this has worse agreement, with a mean interacting distance of 12 Å obtained. This is perhaps unsurprising, as both models assume that the two interacting species have the form factor of an Er(III) ion, and a diffuse semiquinonate

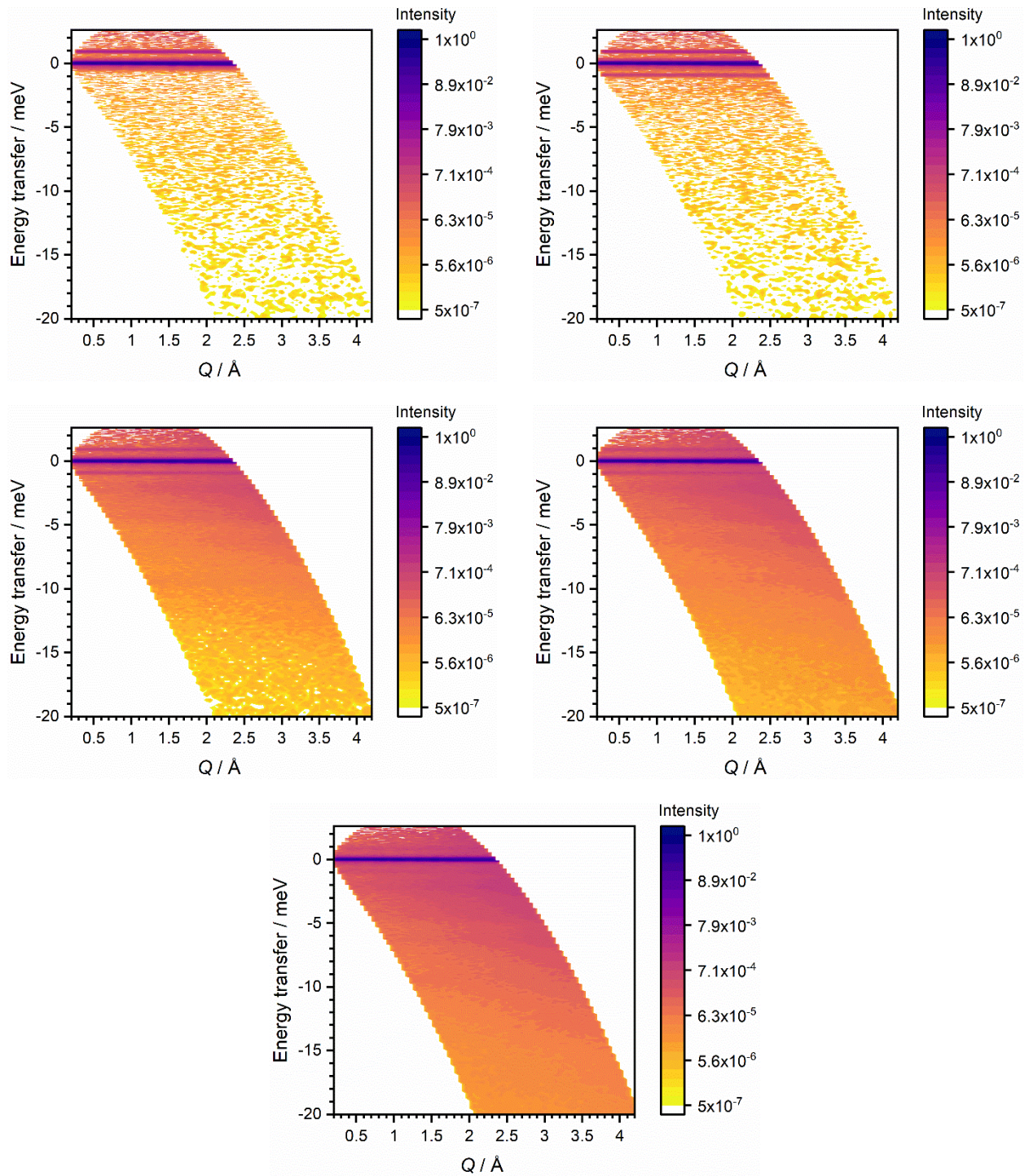radical has a significantly different electron density and therefore expected magnetic form factor.

Figure S13. S(Q,ω) of **Er-dbsq$^{\mathbf{D}}$** measured with $\lambda = 4.69$ Å neutrons, normalised to vanadium and corrected for the Al can background, at $T = 1.5$ K (top left), 10 K (top right), 50 K (middle left), 70 K (middle right), 100 K (bottom).

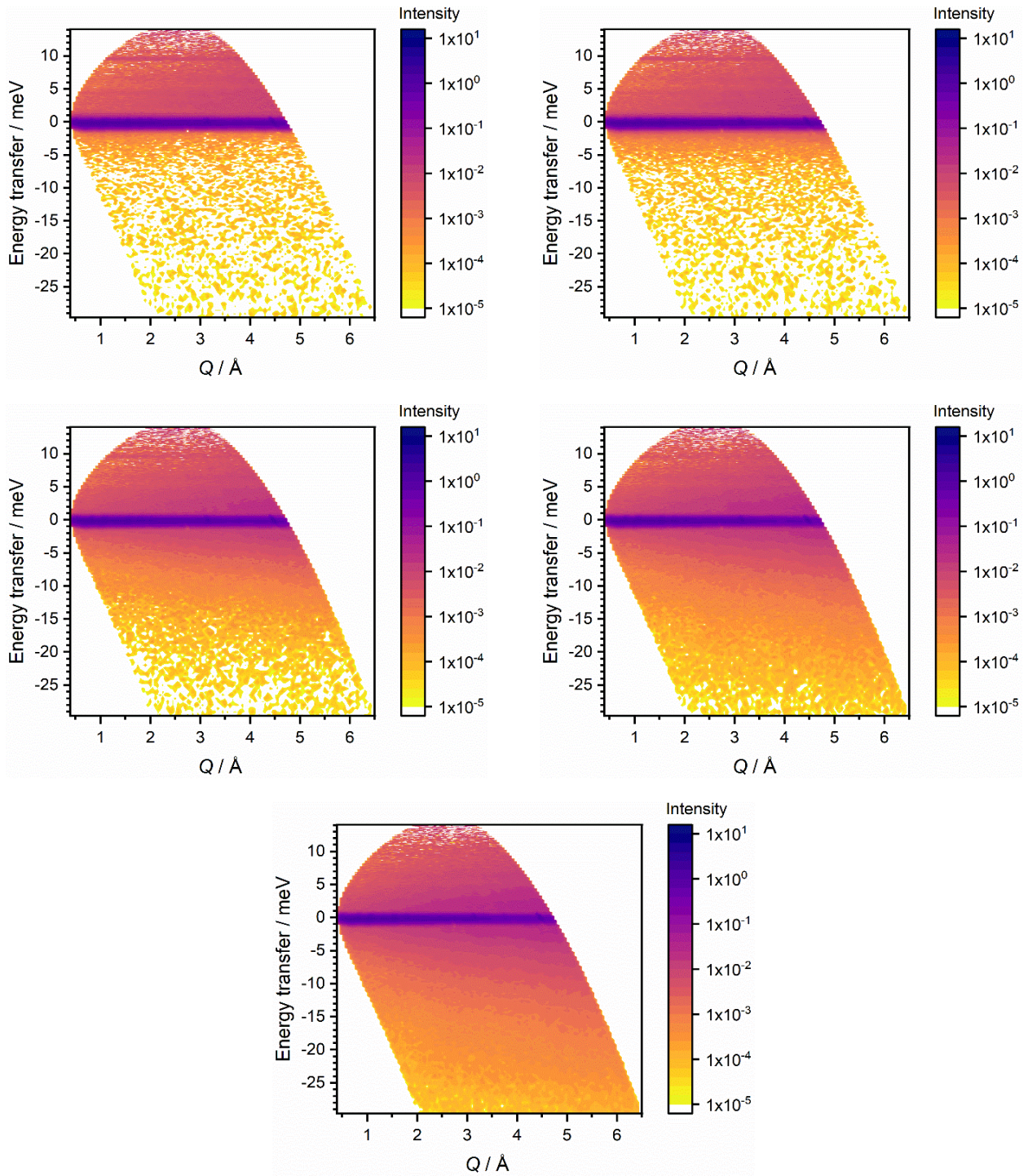**Figure S14.** S(Q,ω) of **Er-dbsq^D** measured with λ = 2.34 Å neutrons, normalised to vanadium and corrected for the Al can background, at T = 1.5 K (top left), 10 K (top right), 50 K (middle left), 70 K (middle right), 100 K (bottom).

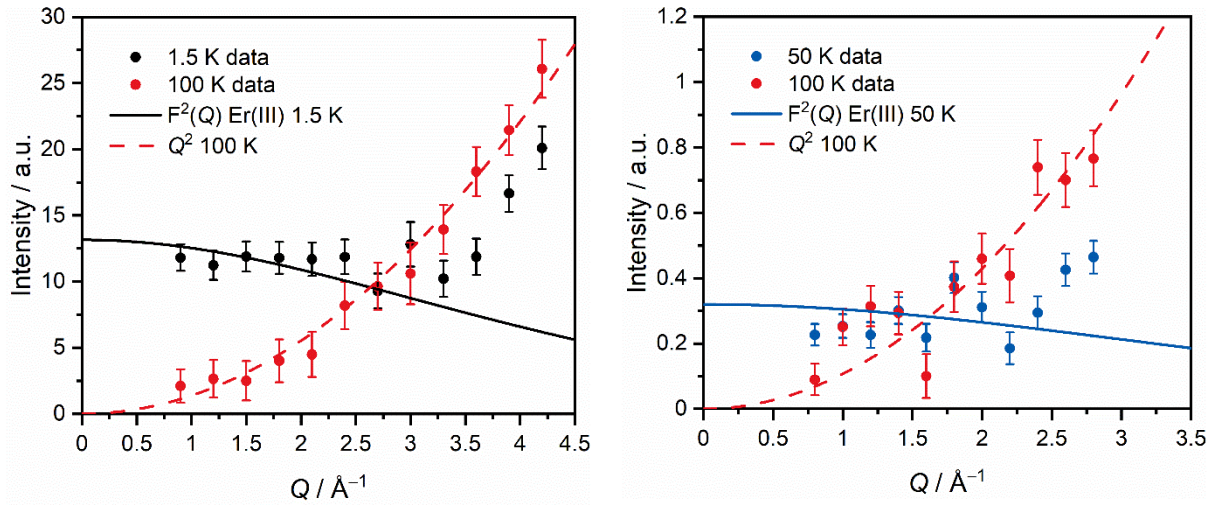**Figure S15.** *Q*-dependence of the transition with $\Delta E = 4.3$ meV for **Er-dbsq^D** with subtraction of **Y-dbsq^D** data. Left: peak **I** at $\lambda = 2.34$ Å, integrated over 3.55 meV $\leq E \leq 5.05$ meV. Right: peak **I'** at $\lambda = 4.69$ Å, integrated over -4.55 meV $\leq E \leq -4.05$ meV. Solid lines demonstrate a CF-like behavior, while dashed lines indicate a phonon-like behavior, scaled to the data at specified temperatures.
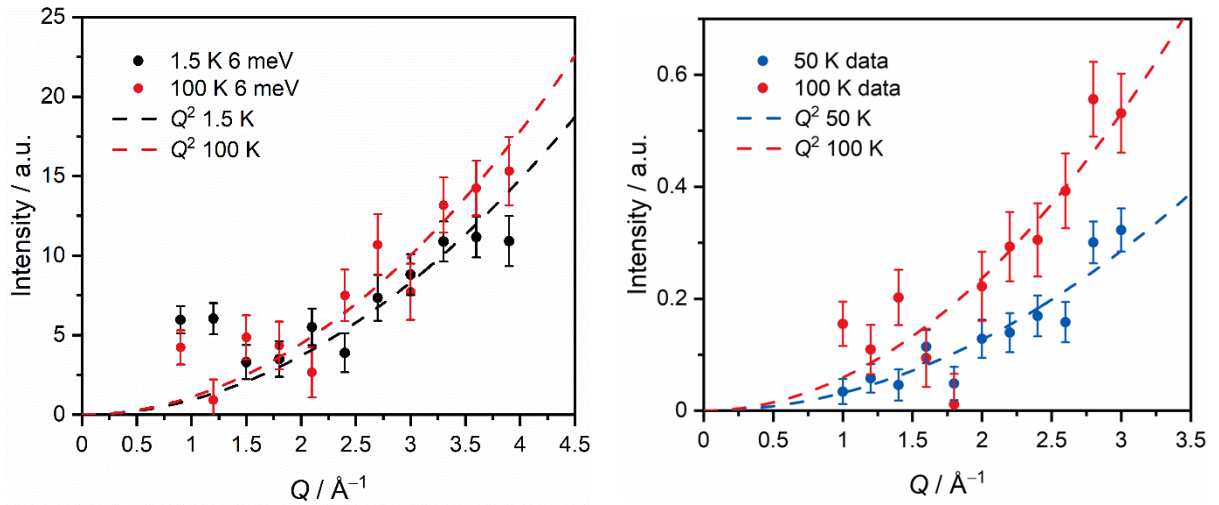

Figure S16. *Q*-dependence of the 6 meV phonon (labelled * in Figure 5 in main text) for **Er-dbsq^D** with subtraction of **Y-dbsq^D** data. Left: $\lambda = 2.34$ Å, integrated over 5.25 meV $\leq E \leq 6.75$ meV. Right: $\lambda = 4.69$ Å, integrated over -6.25 meV $\leq E \leq -5.75$ meV. Dashed lines indicate a phonon-like behavior, scaled to the data at specified temperatures.
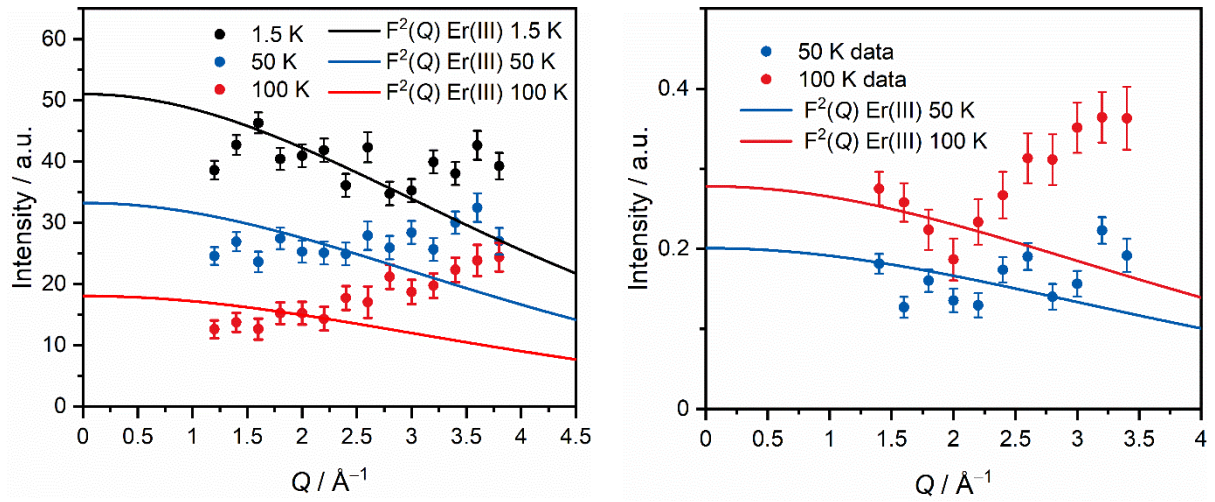
Figure S17. Q-dependence of CF transition with $\Delta E = 9.5$ meV for **Er-dbsq^D** with subtraction of **Y-dbsq^D** data. Left: peak **II** at $\lambda = 2.34$ Å, integrated over 9.0 meV $\leq E \leq 10$ meV. Right: peak **II'** at $\lambda = 4.69$ Å, integrated over -9.75 meV $\leq E \leq -9.25$ meV. Dashed lines indicate a phonon-like behavior, scaled to the data at specified temperatures.

Dynamic magnetic measurements

The dynamic magnetic properties of the Er analogues were probed, as the moderately sized CF splitting between the ground CF state and next highest energy state combined with the large magnetic moment ground state in **Er-trop** might engender slow magnetic relaxation. For 0.075 T, peaks are observed from 2 to 5.5 K within the frequency window measured, while for 0.3 T, a complex profile is observed with measurable maxima from 2 to 6 K (SI Figures 20, 21). The out-of-phase component of the ac magnetic susceptibility was fit using the generalised Debye equation.

Attempts were made to fit the relaxation time with temperature at both fields employing only Orbach relaxation, and these values are reported in Figure S22, however this yields a poor fit. The relaxation rate with temperature was therefore fit using a combination of the Raman relaxation term, direct process and quantum tunnelling of magnetisation:

No direct relaxation was observed in the field dependency of the magnetic relaxation rates for the pure **Er-trop** sample, so was not included in the fits for these data. The relaxation rates at applied fields of 0.075 and 0.3 T were fit to give $C = 0.06(2)$ and $0.22(5)$ s^{-1} K^{-n}, n = 7.5(1) and 6.8(1), $\tau^{-1}_{QTM} = 2.69(9) \times 10^4$ and $6.23(9) \times 10^3$ s^{-1}, respectively. (Figure S19). The rate of QTM is lower at the optimal field, which is expected as the applied magnetic field quenches QTM. There is still a reasonable contribution of QTM at low temperatures, which we attributed as arising from intermolecular dipolar interactions, as observed in the EPR measurements of the undoped compound.

In order to probe the slow magnetic relaxation in the absence of intermolecular interactions, the ac magnetic susceptibility of the doped sample **Er@Y-trop** was measured. A scan of the field dependence of the ac magnetic susceptibility at 2 K (Figure S23) shows no out-of-phase component of the ac magnetic susceptibility in $B_{dc} = 0$ T. An optimal applied field of 0.1 T was chosen for further measurement (Figure S25), and the relaxation rate with temperature fit with equation 3 (Figure 4). The doped sample has a similar higher temperature Raman regime, with comparably sized $C = 0.033(5)$ s^{-1} K^{-n} and $n = 7.9(1)$ obtained from fitting of the relaxation rates. A noticeable decrease in the QTM rate was found shifting the relaxation outside the observable frequency range of the ac measurement. Therefore, the data were fit with no QTM relaxation, however, an additional direct relaxation term was included with $A = 30(3)$ s^{-1} K^{-1}. This decrease in the QTM again suggests the fast QTM relaxation in **Er-trop** originates from transverse dipolar fields due to interactions with neighbouring molecules,

despite the sizeable intermolecular Er⋯Er distance of 9.326 Å. This is not unusual, as Er(III) CF splitting is known to be sensitive to outer-sphere effects.[36]

The dynamic magnetic properties of Er-dbsq were also investigated for comparison with **Er-trop**. As might be expected from the electronic structure calculations, which show the introduction of the magnetic exchange coupling with the dbsq$^{\bullet-}$ radical leads to loss of a doubly degenerate ground state, no out-of-phase component in the ac magnetic susceptibility at 2.75 K was observed even in applied fields up to 0.3 T. This is in contrast to reported Ln-tetraoxolene compounds $[(LnTp_2)_2\mu\text{-}XAn]^{0/-}$ ($XAn^{2-/3-}$ = dihaloanilate; X = Cl, F),[37,38] which have similar coordination geometry to Er-trop and Er-dbsq at each Ln(III) centre. For those systems the introduction of a weak exchange coupling with the radical tetraoxolene ligand allows for slow magnetic relaxation in zero applied magnetic field for the Dy analogues, possibly due to the odd numbers of electrons. Different behaviour for Dy(III) and Er(III) likely originates from the contrasting CF stabilisation arising from the oblate and prolate electron densities, respectively.
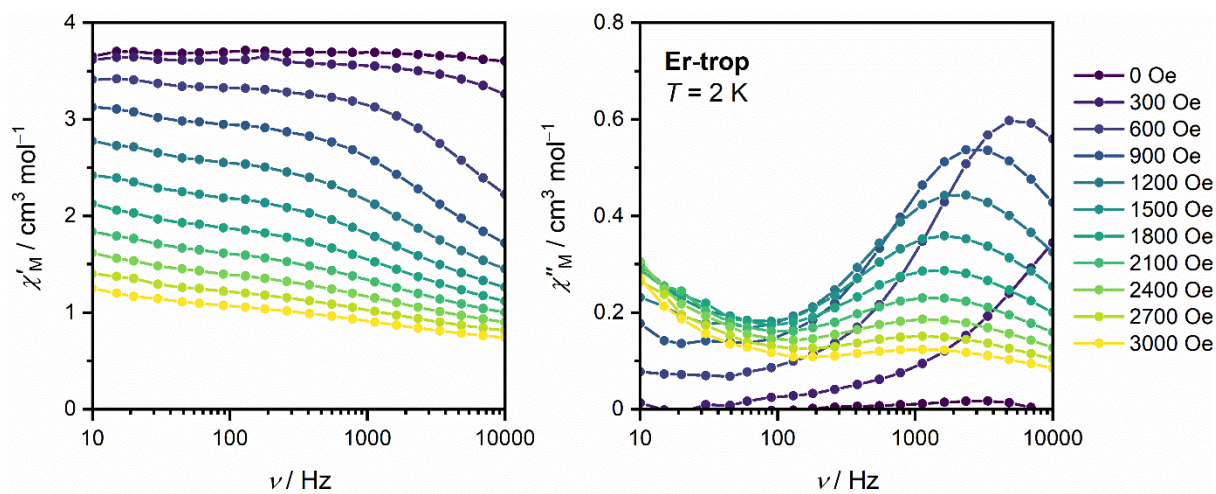
Figure S18. Frequency dependence of the magnetic susceptibility with varying field for **Er-trop** at 2.0 K.
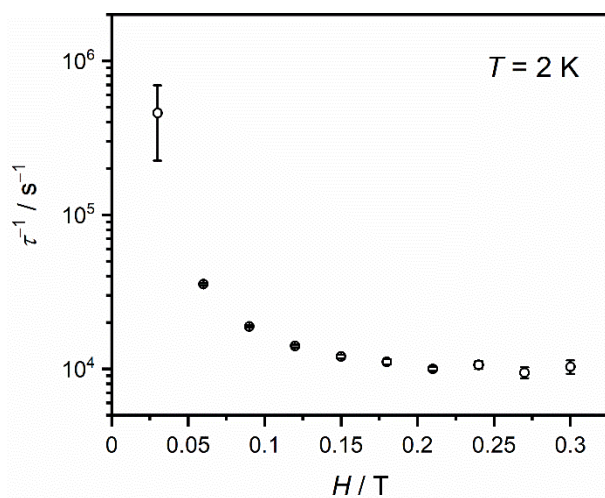

Figure S19. Dependence of the magnetic relaxation rate of **Er-trop** from Debye fitting of the out-of-phase magnetic susceptibility with magnetic field measured at 2.0 K.

Figure S20. Frequency dependence of the magnetic susceptibility with temperature for **Er-trop** measured with $B_{dc} = 0.075$ T.

Figure S21. Frequency dependence of the magnetic susceptibility with temperature for **Er-trop** measured with $B_{dc} = 0.3$ T.

Figure S22. Fitting of relaxation rate with temperature of **Er-trop** with an Orbach-like relaxation process.
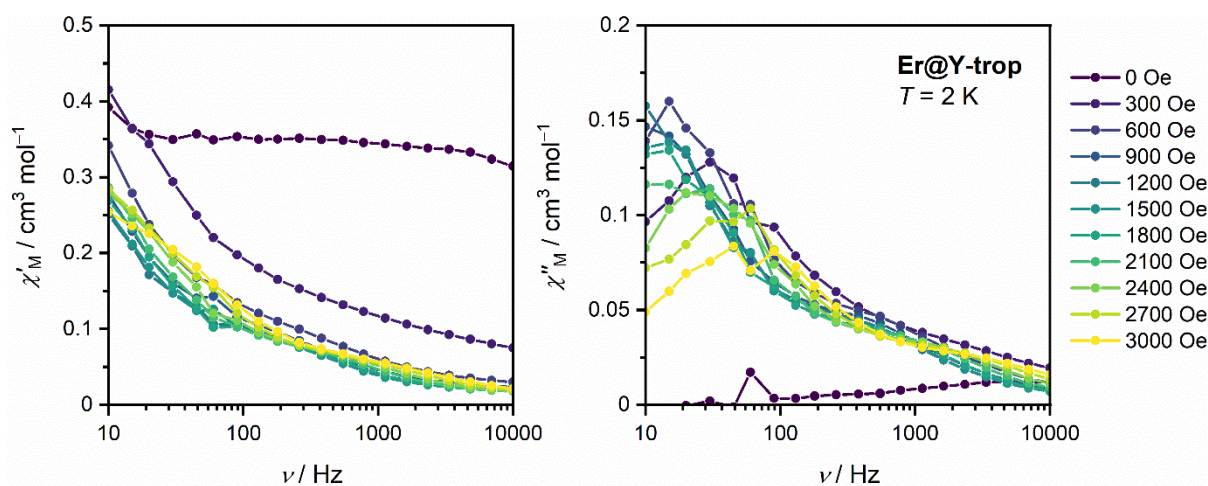
Figure S23. Frequency dependence of the magnetic susceptibility with varying field for **Er@Y-trop** at 2.0 K.

Figure S24. Dependence of the magnetic relaxation rate of **Er@Y-trop** from Debye fitting of the out-of-phase magnetic susceptibility with magnetic field measured at 2.0 K.
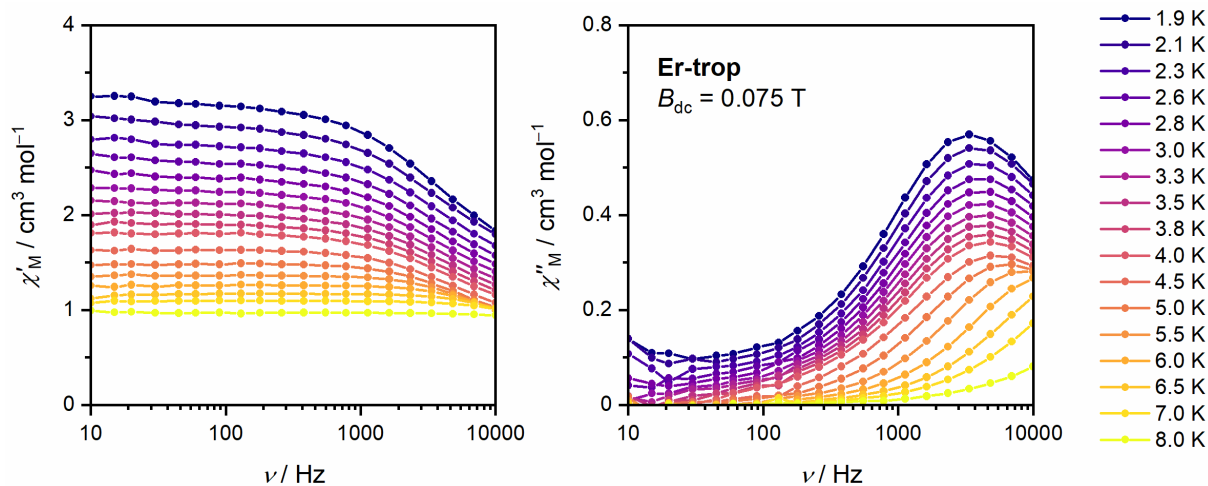

Figure S25. Frequency dependence of the magnetic susceptibility with temperature for **Er-@Y-trop** measured with $B_{dc} = 0.1$ T.
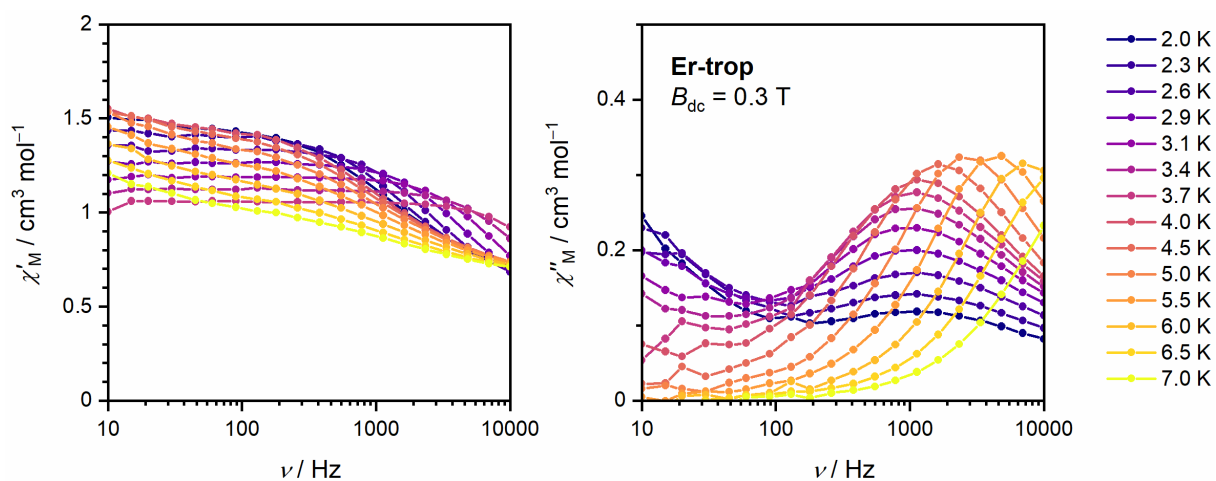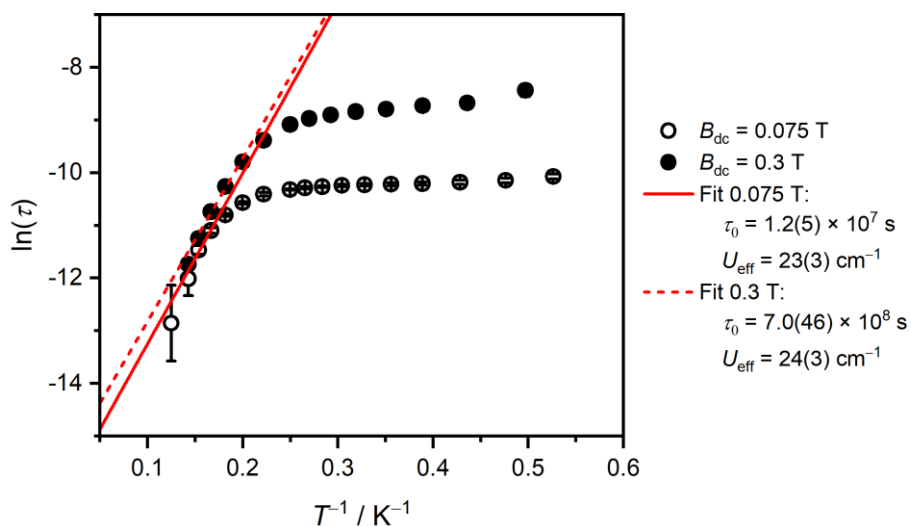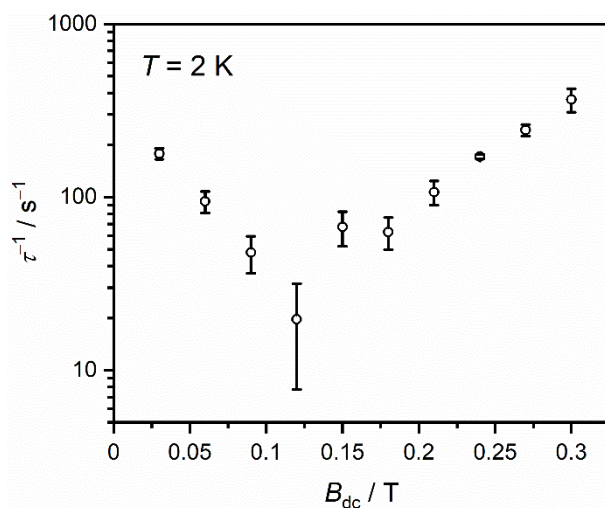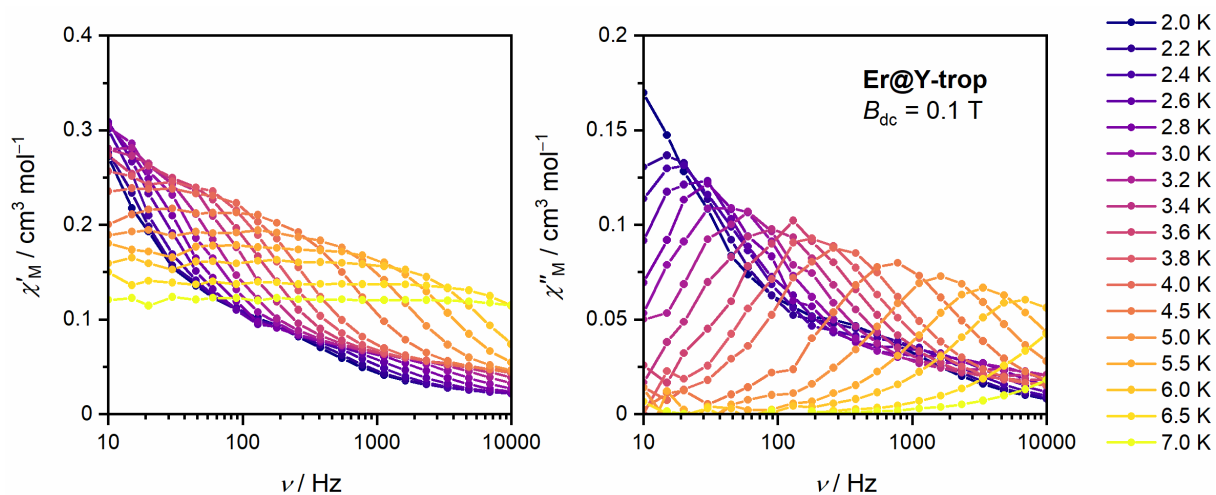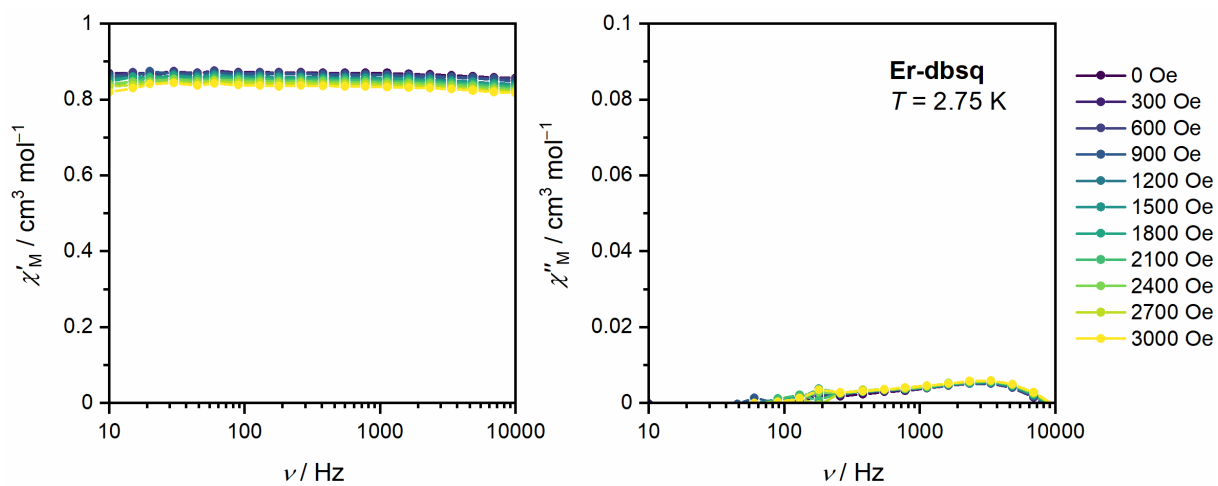
Figure S26. Frequency dependence of the magnetic susceptibility with varying field for **Er-dbsq** at 2.75 K.

Electronic structure calculations

Table S3: Cartesian atomic coordinates (Å) of **Er-trop** used as input for the CASSCF/RASSI-SO *ab initio* calculation

Atom	x	y	z	Atom	x	y	z
Er	0	0	0	C	-0.9117	-2.73548	3.63156
O	-2.05236	0.61501	0.78066	C	2.11142	-0.24002	-4.05154
O	-0.61508	2.05229	-0.7793	C	2.73529	0.91152	-3.6314
N	0.71007	1.54341	1.81933	C	-4.63074	3.20971	0.71849
N	-1.54348	-0.71013	-1.81798	C	-3.20939	4.63105	-0.71698
N	2.3756	-0.52627	0.61338	C	-4.35783	4.35751	-0.00052
N	0.52621	-2.37567	-0.61202	B	1.86894	-0.30719	3.10249
N	-0.25988	-1.26227	2.06636	B	0.307	-1.86912	-3.10233
N	1.26221	0.25982	-2.065	H	0.12314	3.39787	1.32274
N	1.44518	1.1509	2.90537	H	-3.39806	-0.12333	-1.32258
N	-1.15046	-1.44474	-2.90655	H	3.39274	-1.00903	-1.0561
N	2.77943	-0.69735	1.91143	H	1.00884	-3.39293	1.05626
N	0.6978	-2.77899	-1.91261	H	-1.93004	-2.36776	1.85958
N	0.62437	-1.23014	3.10571	H	2.36757	1.92985	-1.85942
N	1.23059	-0.62392	-3.1069	H	-4.26985	1.42691	1.45179
C	-2.56896	1.74858	0.44289	H	-1.4266	4.27017	-1.45028
C	-1.74814	2.5694	-0.44407	H	2.29724	2.20617	4.42582
C	0.59249	2.86482	1.92115	H	2.43044	-0.41679	4.06598
C	-2.86438	-0.59205	-1.92234	H	1.34152	4.23146	3.33269
C	3.38793	-0.99676	-0.12703	H	-2.20586	-2.29693	-4.42432
C	0.99721	-3.38749	0.12584	H	0.41711	-2.43012	-4.06448
C	-1.19315	-2.15627	2.38603	H	-4.23114	-1.34121	-3.33118
C	2.15671	1.19359	-2.38721	H	4.48703	-1.45107	2.71804
C	-3.86994	2.07728	0.9201	H	5.22645	-1.84155	0.38199
C	-2.07747	3.86975	-0.91995	H	1.45138	-4.48671	-2.71653
C	1.79095	2.223	3.64517	H	1.84187	-5.22613	-0.38048
C	1.26556	3.34891	3.04998	H	0.68123	-2.27131	4.85569
C	-2.22319	-1.79114	-3.64501	H	-1.39586	-3.39438	4.07571
C	-3.3491	-1.26575	-3.04982	H	2.27163	-0.68091	-4.85418
C	4.00465	-1.24981	1.94906	H	3.3947	1.39617	-4.0742
C	4.42359	-1.46555	0.66141	H	-5.46325	3.19801	1.13152
C	1.24962	-4.00484	-1.9489	H	-3.19832	5.46294	-1.13256
C	1.46536	-4.42378	-0.66125	H	-5.01559	5.01578	0.00015
C	0.23983	-2.11161	4.0517				

Table S4: Crystal Field Energies for **Er-trop** as obtained from CASSCF/RASSI-SO calculations (cm^{-1}) and decomposition of the wavefunction in the frame of the ground doublet.

Energy (cm^{-1})	g_x	g_y	g_z	Angle	Wavefunction
0	0.45	0.59	14.70	--	9.3|±15/2>, 67.5|±13/2>, 14.6|±11/2>
65.45	0.01	0.02	17.31	4.63	83.5|±15/2>, 10.3|±13/2>
91.97	0.52	0.58	12.54	69.92	17.9|±11/2>, 18.3|±5/2>, 37.7|±3/2>, 18.9|±1/2>
162.14	3.06	6.38	7.03	89.29	7.2|±13/2>, 23.6|±11/2>, 15.0|±9/2>, 47.8|±1/2>
229.61	1.55	3.59	7.98	18.40	9.8|±13/2>, 22.5|±11/2>, 16.3|±7/2>, 11.4|±5/2>, 12.9|±3/2>, 23.4|±1/2>
281.34	1.49	2.18	8.16	20.11	5.8|±11/2>, 43.8|±9/2>, 5.3|±7/2>, 11.0|±5/2>, 21.3|±3/2>, 8.2|±1/2>
333.42	0.54	5.55	7.44	4.04	14.0|±11/2>, 23.6|±9/2>, 40.6|±7/2>, 16.4|±3/2>
374.13	1.41	7.99	8.29	40.43	11.0|±9/2>, 30.3|±7/2>, 46.9|±5/2>, 8.6|±3/2>

Table S5: Crystal Field Parameters obtained from CASSCF/RASSI-SO calculations including operator equivalent factors in the basis of the principal axis of the ground doublet state for **Er-trop** in cm^{-1}.

k	q	CFP (cm^{-1})
2	-2	2.838×10^{-4}
2	-1	2.884×10^{-1}
2	0	-1.126
2	1	-9.791×10^{-4}
2	2	7.593×10^{-1}
4	-4	-1.970×10^{-5}
4	-3	-2.418×10^{-2}
4	-2	-1.929×10^{-5}
4	-1	2.343×10^{-2}
4	0	-2.984×10^{-3}
4	1	1.806×10^{-5}
4	2	-3.354×10^{-5}
4	3	1.447×10^{-4}
4	4	8.683×10^{-3}
6	-6	-3.142×10^{-7}
6	-5	-1.368×10^{-4}
6	-4	-5.508×10^{-7}
6	-3	-2.211×10^{-4}
6	-2	9.575×10^{-8}
6	-1	-5.325×10^{-4}
6	0	5.235×10^{-5}
6	1	-7.358×10^{-7}
6	2	-1.694×10^{-4}
6	3	1.298×10^{-7}
6	4	3.376×10^{-4}
6	5	3.909×10^{-6}
6	6	-1.220×10^{-4}

Table S6: Cartesian atomic coordinates (Å) of **Er-dbsq** used as input for the CASSCF/RASSI-SO ab initio calculation.

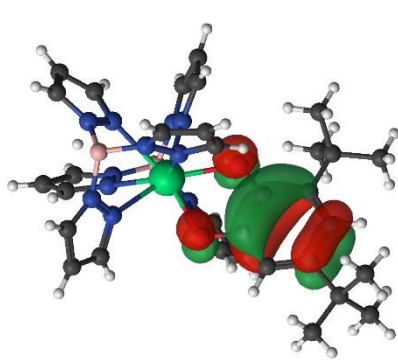| Atom	x	y	z	Atom	x	y	z
Er	0.0	0.0	0.0	H	-3.80057	2.21245	0.33617
O	-2.241	0.43291	-0.09849	H	-5.27981	2.56111	0.83749
O	-0.91595	-1.00759	-1.86072	H	-4.92463	2.63637	-0.72111
N	1.85532	-0.26302	-1.56389	C	-1.26989	2.56904	-2.1141
N	2.50197	2.35764	-0.16743	H	-2.171	2.31153	-1.95861
N	2.57015	0.76168	-2.11062	C	-0.93683	0.44332	4.46922
N	0.88768	2.63167	-2.06273	H	-0.93514	0.09628	5.35352
N	1.65551	1.73863	0.71262	C	-5.99857	-2.67035	-4.14438
N	-0.95585	-2.13732	0.88991	H	-5.52719	-3.46027	-3.80622
N	-0.9211	-2.42667	2.2292	H	-6.5545	-2.92468	-4.91024
N	1.41985	-1.62363	2.6477	H	-6.56689	-2.30126	-3.43638
N	-0.19895	1.95181	-1.58263	C	3.25995	-1.08495	-3.11408
N	1.69298	-1.14535	1.40206	H	3.7205	-1.693	-3.68048
N	-0.69128	0.58019	2.26841	C	3.22369	2.88056	1.85436
N	-0.53846	-0.21809	3.36553	H	3.72468	3.24972	2.57224
C	-4.92596	-0.4765	-2.30915	C	3.41488	0.27909	-3.0434
H	-5.86693	-0.39099	-2.40778	H	4.01741	0.79579	-3.56525
C	-2.85099	-1.32967	-3.20967	C	-4.88744	-0.08807	1.25916
H	-2.36615	-1.7972	-3.87963	H	-5.12732	-1.03041	1.13631
C	-4.19595	-1.13702	-3.35587	H	-5.42808	0.29456	1.98191
C	-2.17237	-0.83606	-2.06369	H	-3.938	-0.01974	1.49003
C	0.49067	3.64239	-2.85954	C	-4.05074	-2.22569	-5.63972
H	1.0627	4.25707	-3.30382	H	-3.3947	-1.55645	-5.92621
C	-4.34838	0.03823	-1.17688	H	-4.58162	-2.51406	-6.41126
C	-5.71405	-0.41327	-5.20693	H	-3.58397	-2.99789	-5.25728
H	-6.36934	-0.06391	-4.56757	C	-5.15612	0.68447	-0.04654
H	-6.17481	-0.70115	-6.0226	C	-1.79659	-3.04048	0.35709
H	-5.0669	0.28881	-5.42796	H	-2.01214	-3.09357	-0.56671
C	-0.88352	3.63361	-2.92134	C	3.03108	-1.18507	1.28426
H	-1.4453	4.22504	-3.40824	H	3.51216	-0.90912	0.51307
C	-1.18472	1.73982	2.7234	C	3.61807	-1.68477	2.44357
H	-1.39531	2.48759	2.17666	H	4.54318	-1.81329	2.61693
C	2.56285	-1.95062	3.28075	C	-1.73216	-3.46357	2.50035
H	2.62799	-2.30586	4.15953	H	-1.88029	-3.84179	3.35908
C	2.1078	2.05862	1.93508	C	-6.65605	0.62645	-0.33371
H	1.71604	1.76188	2.7481	H	-6.85257	1.12919	-1.15156
C	3.44401	3.04256	0.50984	H	-7.14853	1.01903	0.41732
H	4.1445	3.55307	0.12103	H	-6.93076	-0.30751	-0.45097
C	-1.34729	1.70084	4.10538	B	2.3229	2.2245	-1.68961
H	-1.67055	2.39217	4.67113	H	3.05165	2.89445	-2.21365
C	-2.9183	-0.08227	-1.05714	C	-2.31051	-3.88443	1.33022
C	2.27858	-1.37728	-2.17203	H	-2.92638	-4.59755	1.21232
H	1.95291	-2.25003	-1.98579	B	-0.01768	-1.65963	3.21451
C	-4.97649	-1.61366	-4.58277	H	-0.02056	-2.17136	4.2108
C	-4.75392	2.15666	0.11626				
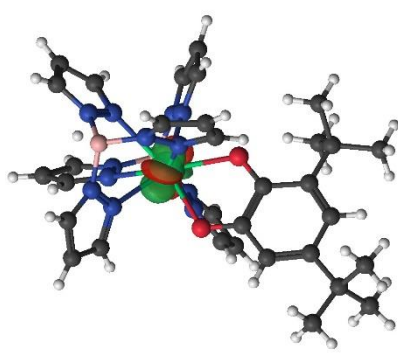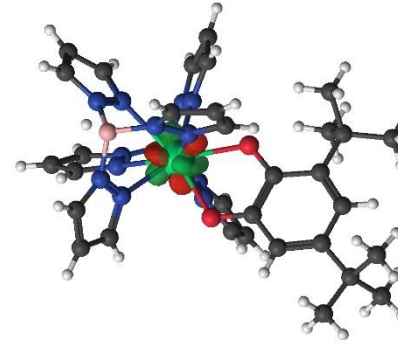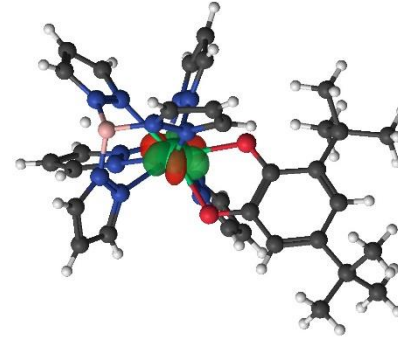
Table S7: Crystal Field Energies of **Er-dbsq** obtained from CASSCF/RASSI-SO calculations (cm^{-1}).

0.00	321	6289	10809	14466	22239	25647	28411	31602	38011
2.35	326	6292	10809	14495	22261	25648	28462	32480	38026
10.2	329	6337	10823	14502	22274	25649	28462	32480	38028
10.3	359	6341	10827	14534	22276	25651	28463	32494	38032
63.3	361	6343	10844	21823	22276	25652	28464	32496	38035
64.4	370	6344	10869	21823	22281	25654	28538	32533	38039
69.8	380	6354	10879	21835	22314	25655	28541	32546	38061
70.0	6117	6356	10904	21836	22317	25730	28541	32562	38080
87.4	6118	6359	10908	21848	22344	25731	28545	32595	38089
89.8	6121	6365	13252	21866	22365	25737	30424	32601	40220
90.3	6121	10038	13270	21876	22420	25740	30425	32615	40222
92.2	6169	10038	13311	21906	22422	27453	30428	32619	40260
164	6171	10094	13322	21942	25541	27456	30429	32675	40284
165	6172	10095	13331	21943	25543	27512	30554	32675	40306
168	6174	10123	13379	21955	25543	27523	30558	35455	40310
176	6214	10124	13424	21979	25544	27553	30568	35456	40346
195	6216	10142	13479	21995	25619	27592	30568	35461	42060
196	6220	10146	13493	21998	25620	27594	31320	35462	42075
202	6223	10165	14229	22021	25627	27624	31328	35468	42111
204	6255	10193	14239	22026	25628	27648	31369	35471	42124
260	6255	10203	14252	22062	25635	27666	31423	35489	42133
261	6260	10211	14258	22062	25636	27696	31444	35490	
263	6263	10213	14305	22118	25636	28404	31461	35494	
272	6281	10726	14348	22119	25637	28405	31474	35495	
321	6282	10726	14397	22236	25637	28407	31550	35501	

Table S8: Energies of **Er-dbsq** obtained from a Lines model exchange applied onto the **Er-trop** CFP energies (cm^{-1}) with J_{ex} = -1.8 cm^{-1}.
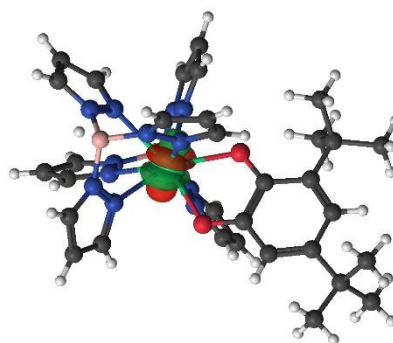
0.00	92.7	230	334
0.29	93.0	232	336
4.55	96.7	233	337
4.59	96.8	234	338
65.6	163	283	374
65.6	166	283	377
70.8	166	285	377
70.8	167	286	379

Table S9. Active space orbitals and average occupation from the RASSCF calculation for the 30 quintet states

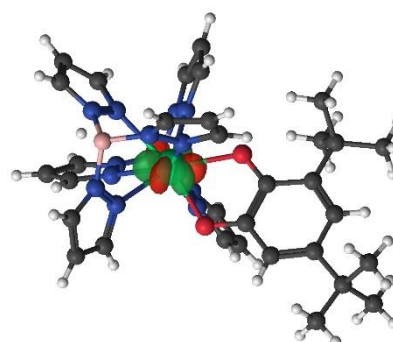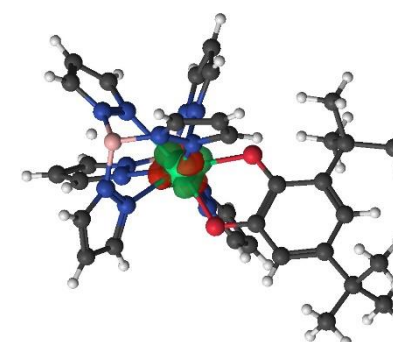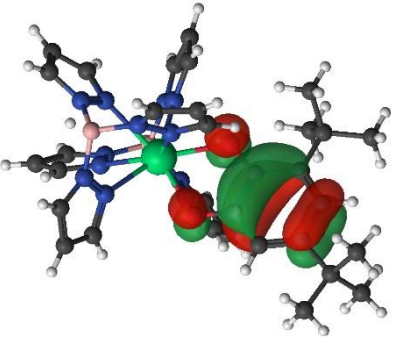| Orbital Number	Average occupation	Rendering
200	1.00	
201	1.57	
202	1.57	
203	1.57	

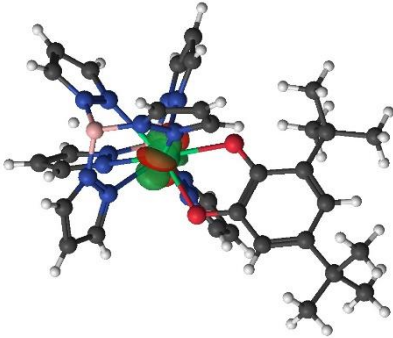204   1.57

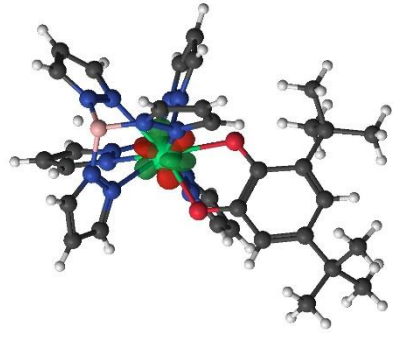205   1.57
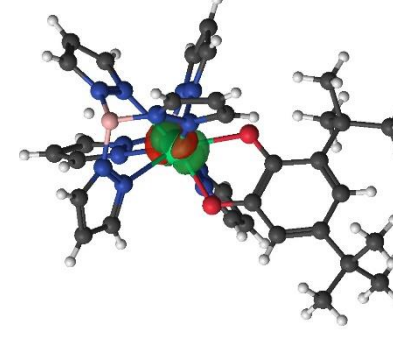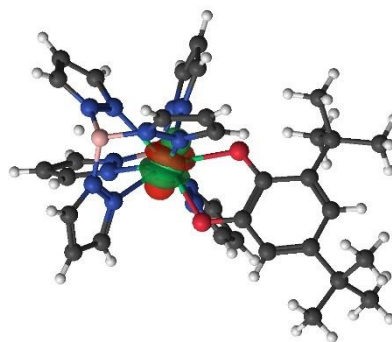
206   1.57

207   1.57
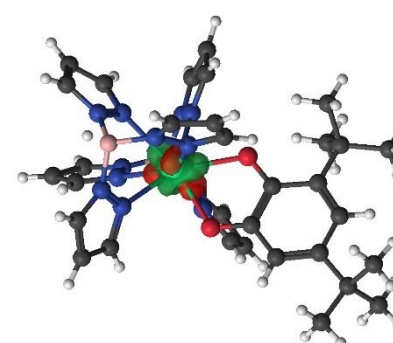
Table S10. Active space orbitals and average occupation from the RASSCF calculation for the 32 triplet states

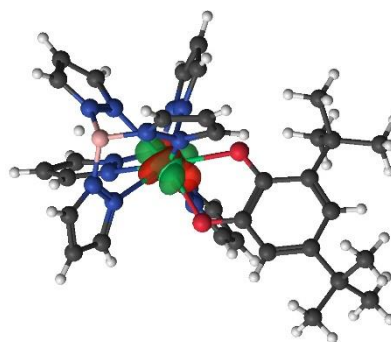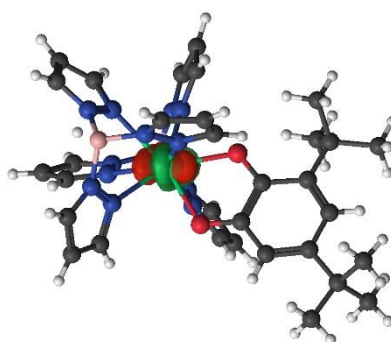| Orbital Number	Average occupation	Rendering
200	1.00	
201	1.58	
202	1.58	
203	1.57	

204 1.57

205 1.57

206 1.57

207 1.56
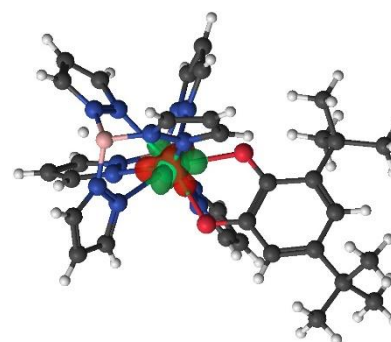
Table S11. Calculated energies of pseudo-doublets for **Er-dbsq** with the effective *g*-tensor values from Single_Aniso

Pseudo-doublet energies (cm^{-1})	Pseudo-doublet energies (meV)	g_x value	g_y value	g_z value
0/2.35	0/0.29	0.00	0.00	12.85
10.2/10.3	1.27/1.28	0.00	0.00	16.94
63.3/64.4	7.84/7.99	0.00	0.00	14.77
69.8/70.0	8.66/8.67	0.00	0.00	19.07
87.4/89.8	10.84/11.13	0.00	0.00	9.64
90.3/92.2	11.20/11.43	0.00	0.00	5.04
163.6/165.1	20.29/20.46	0.00	0.00	11.24
167.7/176.0	20.79/21.82	0.00	0.00	7.07

Q-dependence Modelling

The lowest energy transition in the INS spectrum of **Er-dbsq**, centred at 0.918 meV, has an energy that is comparable to the *ab initio* energy gap between the ground and first excited state tunnel-split Ising pseudo-doublets, resulting from the exchange coupling of the Er(III) ground Kramers Doublet (KD) and the dbsq-radical spin. The measured powder-averaged *Q*-dependence displays an oscillatory and slowly decaying behaviour (Figure S27), not expected of a typical 4*f*-based INS transition. Such a transition could, in principle, be generated solely by the spin-flip excitation of the semiquinonate radical moiety, an inelastic process with an energy cost of the order of the exchange coupling between the radical and the Er 4*f* electrons.

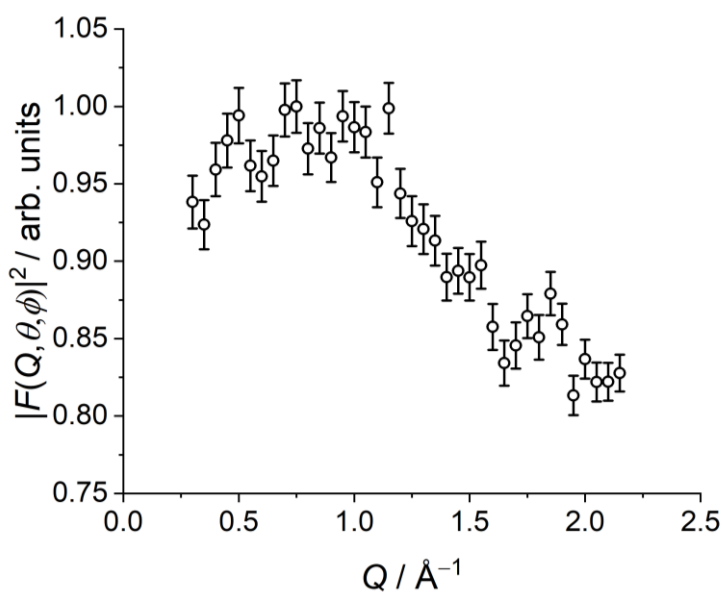**Figure S27:** Experimental dependence of the powder-averaged form factor for the 0.918 meV INS transition on the neutrons momentum transfer *Q*.

Here, we deploy a model to simulate the observed *Q*-dependence of the low-energy INS transition. The starting point is a decomposition of the *ab initio* wavefunctions associated to the two pseudo-doublets into their radical and Er crystal field components, achieved by

assuming that the crystal field component of the **Er-dbsq** Hamiltonian is well described by the *ab initio* crystal field Hamiltonian of the **Er-trop** complex, and that the exchange-coupling Hamiltonian can be described by an anisotropic spin-spin coupling model. This scenario is addressed as Model 2 in what follows. Before discussing Model 2, we first introduce Model 1 (with detail below), which describes the idealised assumption that the INS transition is solely determined by the radical spin-flip excitation. We then develop a computational scheme to calculate the form factor for the pure radical based transition from the *ab initio* wavefunction and use it to show that Model 1 fails to describe the observed Q-dependence. This indicates that the associated excitation cannot be described as a pure dbsq-radical based spin-flip transition. However, by switching to the more realistic Model 2 and extending the methodology for the calculation of the form factor calculation to the case of a general wavefunction resulting from the anisotropic exchange coupling between substantially m_J-mixed crystal field states and the dbsq radical, we show that the dbsq-based spin-flip excitation is pivotal in describing the observed transition, by virtue of its interference (coherent superposition) to the Er-based $4f$-excitations.

Model 1: The pure radical-based spin-flip INS transition

We know from *ab initio* calculations that the ground KD of the **Er-trop** complex is dominated by the $|m_J = \pm 13/2\rangle$ doublet (68%), with the first excited state at more than 64 cm^{-1} (8.09 meV) and dominated by a $|m_J = \pm 15/2\rangle$ doublet. If we assume that **Er-trop** is a reasonable model for the crystal field Hamiltonian in **Er-dbsq**, the simplest possible model for the two lowest energy pseudo-doublets of **Er-dbsq** can be cast in terms of a ground antiferromagnetic doublet $|m_J = \pm 13/2, m_s = \mp 1/2\rangle \equiv \{|\Uparrow\downarrow\rangle, |\Downarrow\uparrow\rangle\}$ tunnel-split into $\{|\mathbf{1}\rangle, |\mathbf{2}\rangle\} \equiv 2^{-1/2}(|\Uparrow\downarrow\rangle \pm |\Downarrow\uparrow\rangle)$, and separated from the tunnel-split ferromagnetic pseudo-doublet $\{|\mathbf{3}\rangle, |\mathbf{4}\rangle\} \equiv$

$2^{-1/2}(|\Uparrow\uparrow\rangle \pm |\Downarrow\downarrow\rangle)$ by a gap of about $\Delta_{\text{exch}} \approx 10$ cm^{-1} (1.25 meV), as determined by *ab initio* calculations (see Figure S28 for a schematic representation).
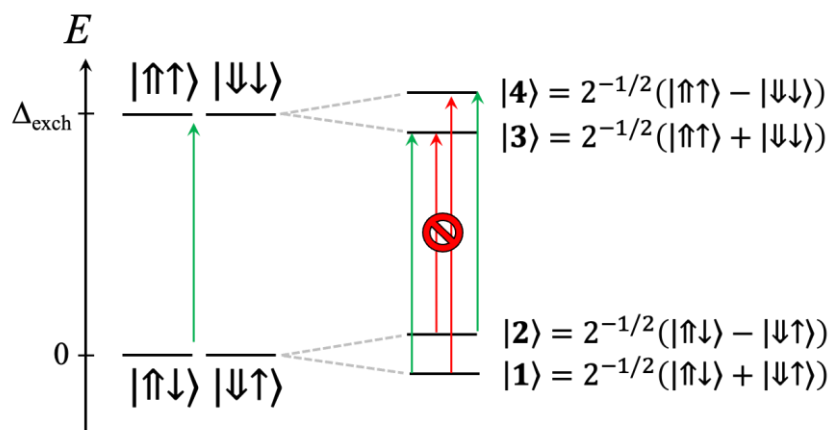

Figure S28: Schematic representation of the low-energy spectrum for **Er-dbsq**, where each state is approximated as the dbsq radical spin antiferromagnetically coupled to a pure $|m_J = \pm 13/2\rangle$ ground Kramers doublet, dominating the *ab initio* ground Kramers doublet found for the **Er-trop** analogue.

If the splitting of the two Ising doublets were of equal magnitude, the two INS-allowed spin flip transitions $1 \rightarrow 3$ and $2 \rightarrow 4$ would have the same exact energy and therefore give rise to a single INS absorption peak. Calculations show in fact that the $\Delta_{1,2} \approx 0.3$ meV (2.34 cm^{-1}), while the second gap is vanishingly small ($\Delta_{3,4} \approx 0.97$ x 10^{-5} meV/ 0.079 cm^{-1}). Hence, in principle we could expect two transitions: $\Delta_{1 \rightarrow 3}$ =1.26 meV, and $\Delta_{2 \rightarrow 4}$ =0.978 meV.

Calculation of the magnetic neutron scattering form factor for Model 1

Model 1 is the typical scenario where the only magnetic transition induced by neutron scattering is the pure dbsq-radical based spin-flip excitation (since $\Delta m_J > 1$ for other transitions). In such a process only the spin-term survives in the calculation of the INS

scattering cross section $S(\omega, \mathbf{Q})$ for all transitions between the antiferromagnetic ground pseudo-doublet (AF =1, 2) and the ferromagnetic excited pseudo-doublet (F = 3,4):

$$S(\omega, \mathbf{Q}) \propto \sum_\alpha^{x,y,z} \left| \left\langle F \left| \left\{ \mathbf{u}_Q \times \left[\left(\sum_{j=1}^{N_{el}} \hat{\mathbf{s}}_j \, e^{i\mathbf{Q}\cdot\mathbf{r}_j} \right) \times \mathbf{u}_Q \right] \right\}_\alpha \right| AF \right\rangle \right|^2 \qquad \text{(S3)}$$

Here $\mathbf{u}_Q = \mathbf{Q}/Q$ is a unit vector pointing in the direction of the neutron's momentum transfer $\mathbf{Q}$, while $\mathbf{r}_j$ is the position and $\hat{\mathbf{s}}_j$ the spin of the jth-electron. It can be shown that the transition matrix element simplifies to:

$$\left\langle F \left| \mathbf{u}_Q \times \left[\left(\sum_{j=1}^{N_{el}} \hat{\mathbf{s}}_j \, e^{-i\mathbf{Q}\cdot\mathbf{r}_j} \right) \times \mathbf{u}_Q \right] \right| AF \right\rangle = 2\, F_{\text{dbsq}}(\mathbf{Q}) \left[\langle \downarrow |\mathbf{s}| \uparrow \rangle - \mathbf{u}_Q (\langle \downarrow |\mathbf{s}| \uparrow \rangle \cdot \mathbf{u}_Q) \right] \text{ (S4)}$$

where the complex-valued structure factor $F(\mathbf{Q})$, for this particular case, is the Fourier transform of the π-molecular orbital hosting the dbsq spin density (the π-SOMO):

$$F_{\text{dbsq}}(\mathbf{Q}) = \int d\mathbf{r}\, \left| \phi_{\pi,\text{SOMO}}(\mathbf{r}) \right|^2 e^{i\mathbf{Q}\cdot\mathbf{r}} \qquad \text{(S5)}$$

If we choose the electronic spin quantization axis of the π-SOMO to lie in a direction parallel to the magnetic anisotropy axis of the **Er-dbsq** complex, the factor $2\big[\langle \downarrow |\mathbf{s}| \uparrow \rangle - \mathbf{u}_Q(\langle \downarrow |\mathbf{s}| \uparrow \rangle \cdot \mathbf{u}_Q)\big] = 1 + u_{Q,z}^2 \equiv 1 + \cos^2 \theta_Q$, where θ_Q is the angle formed by the momentum transfer vector with the magnetic anisotropy axis of **Er-dbsq**.

Thus, the powder averaged experimental form factor can be modelled as:

$$\left|F_{\mathrm{dbsq}}(Q)\right|^2 \propto \int d\phi_Q d\theta_Q \sin\theta_Q \left(1 + \cos^2\theta_Q\right)^2 \left|\int d\mathbf{r}\, \left|\phi_{\pi,\mathrm{SOMO}}(\mathbf{r})\right|^2 e^{i\mathbf{Q}\cdot\mathbf{r}}\right|^2 \qquad (S6)$$

We have implemented Eq. S6 using the *ab initio* molecular orbital $\phi_{\pi,\mathrm{SOMO}}(\mathbf{r})$ calculated with an ANO-RCC-TZP Gaussian-Type Orbital (GTO) basis set. In the calculations we neglected any atomic centre on which the π-SOMO has an LCAO amplitude smaller than 0.01, i.e. we only keep three $2p_z$ GTO-functions and the two $3d_{xz}$ and $3d_{yz}$ polarization GTO-functions on the six C atoms and two O atoms of the dbsq moiety, plus the equivalent GTO-functions for the Er atom. The results are plotted in Figure S29, and they show that this model is too simple to explain the observe Q-dependence.
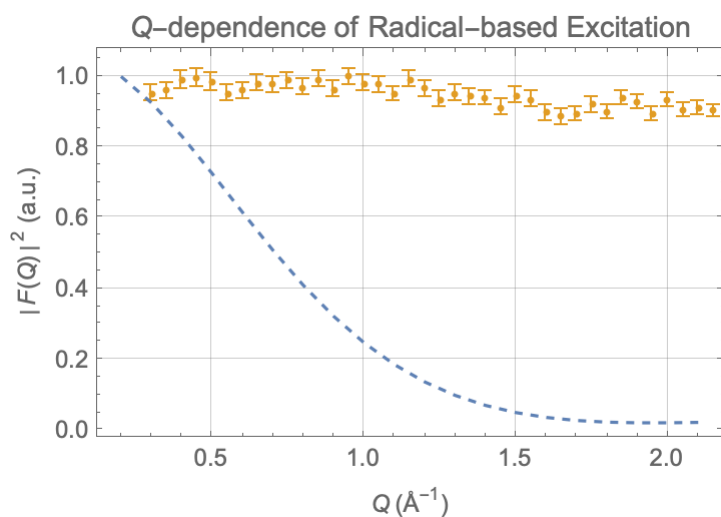

Figure S29. *Ab initio* form factor calculated via an implementation of Eq. (4), where the π-SOMO molecular orbital is taken from ANO-RCC-TZP calculations (blues dashed line), compared with experimental form factor (orange data points with experimental error bars).

Model 2 (full ab initio wavefunction modelled via the tropolonate-analogue): Interference between radical-spin-flip and Ln-based INS transitions

Next, we proceed to build an improved model of the four transitions with energy gaps close to the measured 0.918 meV INS peak. The new model is based on an _ab initio_ representation of the wavefunctions of the two low energy pseudo-doublets of **Er-dbsq**, instead of approximating them with a pure $|m_J = \pm 13/2\rangle$ Kramers doublet exchange-coupled to the dbsq-radical spin, as presented in Model 1. Since the SINGLE_ANISO module cannot perform a meaningful angular momentum decomposition of wavefunctions with two open-shell moieties such as the **Er-dbsq** case, here we model the two pseudo-doublets wavefunctions by diagonalising the _ab initio_ crystal field Hamiltonian calculated via the SINGLE_ANISO module for the **Er-trop** analogue, corrected with an empirical exchange Hamiltonian between the pure spin moment of Er and that of the dbsq-radical, represented on the full 32-dimensional basis $|m_J, m_s\rangle$ with $m_j = \pm 1/2, \pm 3/2, \ldots, \pm 13/2, \pm 15/2$, and $m_s = \pm 1/2$. While the form of the exchange Hamiltonian is of course approximate in nature and hence will not suffice to reproduce all of the 32 _ab initio_ states, here we only aim at a reasonable representation of the two lowest-lying pseudo-doublets (lowest four states), achieved by fitting the exchange parameters, so as to reproduce the four energy levels centred at the 0.918 meV transition.

Interestingly, we find that there is no way to achieve this with an isotropic Heisenberg Hamiltonian. The simplest way we found to approximately reproduce the tunnel splitting and the energy gaps of the four lowest states compatible with the crystal field Hamiltonian of **Er-trop**, was to pick the following anisotropic exchange Hamiltonian:

$$\hat{H}_{exch} = -J_X \hat{S}_{Er,X} \hat{s}_{rad,X} - J_Y \hat{S}_{Er,Y} \hat{s}_{rad,Y} - J_Z \hat{S}_{Er,Z} \hat{s}_{rad,Z} \qquad (S7)$$

With $J_X = -36.5\ \text{cm}^{-1}$, $J_Y = -25.8\ \text{cm}^{-1}$, and $J_Z = -7.75\ \text{cm}^{-1}$, we obtain the energy spectrum for the two pseudo-doublets reported in Figure S30 below, which reproduce the low-energy splitting of the two pseudo-doublets of interest observed in the *ab initio* spectrum and qualitative nature of the m_j wavefunctions from **Er-trop**.

Ab initio (black) Model 2(red)

$|3,4\rangle \sim$ 41% $|\pm 13, \pm\rangle$ + 2.5% $|\pm 5, \pm\rangle$ + 2.3% $|\pm 15, \mp\rangle$ + 1.4% $|\pm 11, \mp\rangle$ + 1% $|\pm 15, \pm\rangle$

$|2\rangle \sim$ 43% $|\pm 13, \mp\rangle$ + 2.4% $|\pm 5, \mp\rangle$ + 1.4% $|\pm 11, \mp\rangle$ + 1.2% $|\pm 15, \mp\rangle$

$|1\rangle \sim$ 42% $|\pm 13, \mp\rangle$ + 2.7% $|\pm 5, \mp\rangle$ + 1.3% $|\pm 11, \mp\rangle$ + 1.0% $|\pm 15, \mp\rangle$
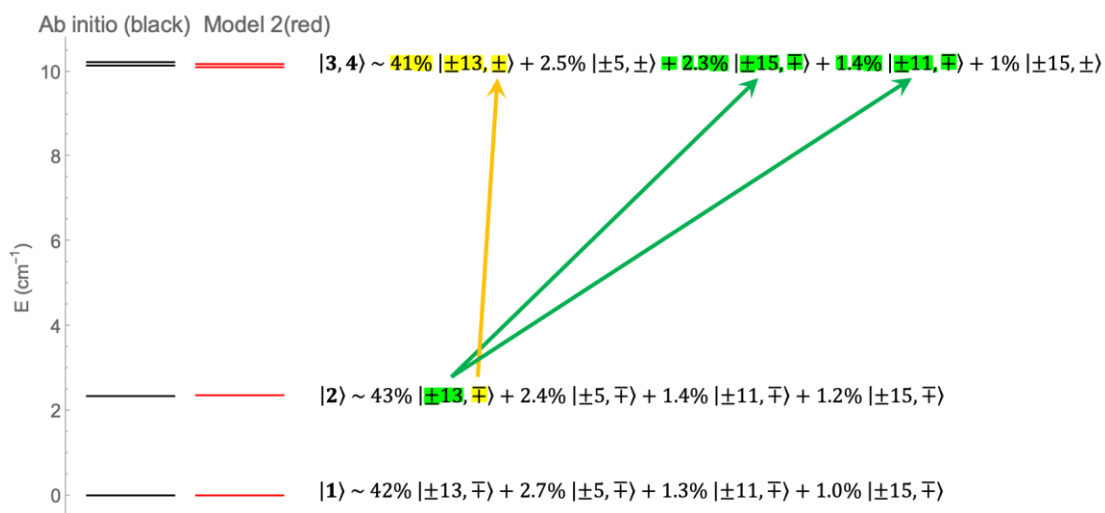
Figure S30. Low-energy spectrum of **Er-dbsq** calculated *ab initio* at the CASSCF/RASSI-SO level (left, black energy levels), and via our Model 2, built by adding an anisotropic exchange Hamiltonian Eq. S7 to the *ab initio* CASSCF/RASSI-SO crystal field Hamiltonian for the **Er-trop** analogue (right, red energy levels). The ensuing wavefunctions decomposition on the $|m_j, m_s\rangle$ basis, obtained from Model 2, is reported beside the levels. The yellow (green) arrow indicates an instance of a radical-centred spin-flip (Er-centred m_j-flip) process contributing to the overall transition matrix element.

We note that the anisotropic terms are necessary also to improve agreement with magnetic data. In Figure S31 we report the plot of the magnetisation vs field at 2K, computed both using an isotropic Heisenberg exchange Hamiltonian with exchange coupling constant $J = -7.45\ \text{cm}^{-1}$ and with Eq. S7. Also, while the sign of J_x and J_y does not influence the energy splitting reported in Figure S30 (provided J_x and J_y have the same sign), their sign influences the

composition of the wavefunctions leading to a significantly improved agreement with experimental data if J_x and J_y are both negative like J_z Figure S31. Finally, the full parameter space was thoroughly searched and the above parameters do not represent a unique solution. Taking the similar parameters $J_X = -32.6 \text{ cm}^{-1}$, $J_Y = -28.8 \text{ cm}^{-1}$, and $J_Z = -7.56 \text{ cm}^{-1}$ gives a comparable splitting, wavefunction description, and comparison to magnetic data.
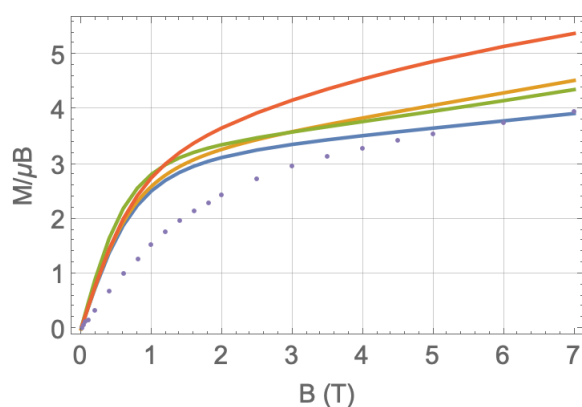

Figure S31. Powder-averaged magnetisation vs applied field at T = 2 K. Experimental values (purple datapoints), *ab initio* calculations (yellow solid line), and our Model 2 using *ab initio* crystal field of **Er-trop** and exchange Hamiltonian Eq. S7, with three different sets of exchange coupling parameters: $J_X = -36.5 \text{ cm}^{-1}$, $J_Y = -25.8 \text{ cm}^{-1}$, and $J_Z = -7.75 \text{ cm}^{-1}$ (blue solid line), $J_X = +36.5 \text{ cm}^{-1}$, $J_Y = +25.8 \text{ cm}^{-1}$, and $J_Z = -7.75 \text{ cm}^{-1}$ (orange solid line), and $J_X = -7.45 \text{ cm}^{-1}$, $J_Y = -7.45 \text{ cm}^{-1}$, and $J_Z = -7.45 \text{ cm}^{-1}$ (green solid line, corresponding to an isotropic Heisenberg Hamiltonian).
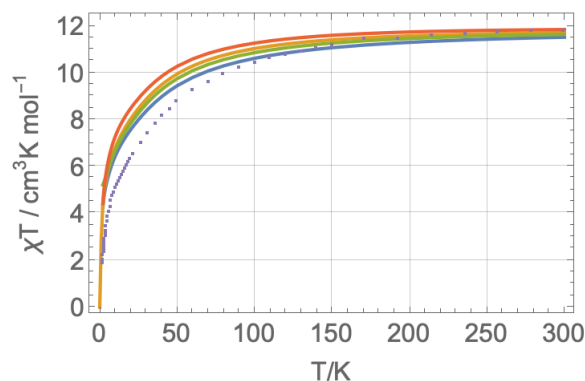
Figure S32. Temperature dependence of the powder susceptibility. Experimental values (purple datapoints), *ab initio* calculations (yellow solid line), and our Model 2 using *ab initio* crystal field of **Er-trop** and exchange Hamiltonian Eq. S7, with three different sets of exchange coupling parameters: $J_X = -36.5$ cm^{-1}, $J_Y = -25.8$ cm^{-1}, and $J_Z = -7.75$ cm^{-1} (blue solid line), $J_X = +36.5$ cm^{-1}, $J_Y = +25.8$ cm^{-1}, and $J_Z = -7.75$ cm^{-1} (orange solid line), and $J_X = -7.45$ cm^{-1}, $J_Y = -7.45$ cm^{-1}, and $J_Z = -7.45$ cm^{-1} (green solid line, corresponding to an isotropic Heisenberg Hamiltonian).

The wavefunctions obtained with Eq. S7 and the *ab initio* crystal field Hamiltonian of **Er-trop** are evidently more involved with respect to the simplified approximations described by Model 1, and they can evidently trigger new INS transition processes. We note in particular that the ferromagnetic excited doublet $|3\rangle, |4\rangle$, besides the expected contributions from $|m_J, m_s\rangle$ configurations with parallel (same sign) m_j and m_s, also features a non-negligible contribution from a configuration in which m_j and m_s are antiparallel (of opposite sign), which can be reached from the lower energy doublet $|1\rangle, |2\rangle$ by flipping one unit of m_j angular momentum. Hence, contributions to the INS transition matrix element can also be triggered from Er-based processes, which, in turn, can cause interference between radical-based spin-flip and Er-based m_j-flip processes, as highlighted in Figure S30.

Calculation of the magnetic neutron scattering form factor for Model 2

S53

To test the effect of these interference processes, we need to generalise Eq. S6 for the INS form factor so that both Er-based transitions and dbsq-radical spin-flip transitions can be included. We start from a general definition of the INS scattering cross section $S(\omega, \boldsymbol{Q})$, now featuring both spin and orbital current contributions to the four possible AF→F transitions:

$$S(\omega, \boldsymbol{Q}) \propto \sum_{\alpha}^{x,y,z} \left| \left\langle \boldsymbol{F} \middle| \left\{ \boldsymbol{u_Q} \times \left[\left(\sum_{j=1}^{N_{el}} e^{i\boldsymbol{Q} \cdot \boldsymbol{r}_j} \left[\hat{\boldsymbol{s}}_j - Q^{-1} \boldsymbol{u_Q} \times \boldsymbol{\nabla}_j \right] \right) \times \boldsymbol{u_Q} \right] \right\}_{\alpha} \middle| \boldsymbol{AF} \right\rangle \right|^2 \quad (S8)$$

Where $-i\hbar\boldsymbol{\nabla}_j$ is the linear momentum differential operator for the jth electron, and $|\boldsymbol{AF}\rangle = \sum_{m_j, m_s} C_{m_j, m_s}^{AF} |m_j, m_s\rangle$ and $|\boldsymbol{F}\rangle = \sum_{m_j, m_s} C_{m_j, m_s}^{F} |m_j, m_s\rangle$ are the lowest four eigenfunctions obtained from our Model 2 (AF = 1,2, F = 3,4, $m_j = -\frac{15}{2} \dots, \frac{15}{2}$, and $m_s = \uparrow, \downarrow$). Expanding Eq. S8 to expose both radical-based and Er-based contributions:

$$F_{\text{tot}}(\boldsymbol{Q}) = \left\langle \boldsymbol{F} \middle| \left\{ \boldsymbol{u_Q} \times \left[\left(\sum_{j=1}^{N_{el}} e^{i\boldsymbol{Q} \cdot \boldsymbol{r}_j} \left[\hat{\boldsymbol{s}}_j - Q^{-1} \boldsymbol{u_Q} \times \boldsymbol{\nabla}_j \right] \right) \times \boldsymbol{u_Q} \right] \right\}_{\alpha} \middle| \boldsymbol{AF} \right\rangle =$$

$$\sum_{m_j, m_j'} \sigma_{m_j' m_j}^{Er, AF \to F} [F_{\text{Er}^{3+}}(\boldsymbol{Q})]_{\alpha m_j m_j'} +$$

$$F_{\text{dbsq}}(\boldsymbol{Q}) \sum_{m_s, m_s'} \sigma_{m_s' m_s}^{dbsq, AF \to F} \left\langle m_s \middle| \{ \boldsymbol{s} - \boldsymbol{u_Q}(\boldsymbol{s} \cdot \boldsymbol{u_Q}) \}_{\alpha} \middle| m_s' \right\rangle \quad (S9)$$

where $\sigma_{m_j' m_j}^{Er, AF \to F} = \left(C_{m_j', \uparrow}^{AF} C_{m_j, \uparrow}^{F*} + C_{m_j', \downarrow}^{AF} C_{m_j, \downarrow}^{F*} \right)$ and $\sigma_{m_s' m_s}^{dbsq, AF \to F} = \left(\sum_{m_j} C_{m_j, m_s'}^{AF} C_{m_j, m_s}^{F*} \right)$ are the reduced transition density matrices for the Er-based and dbsq-based excitations, respectively, describing the 4f-radical spin entanglement properties contained in the exchange-coupled wavefunction. We implemented Eq. S9 by calculating $F_{\text{dbsq}}(\boldsymbol{Q})$ using Eq. S6 above. The *ab initio* π-SOMO LCAO coefficients, and our implementation of the Fourier transform of the overlap matrix elements associated to the ANO-RCC-TZP basis, and now with the more

involved angular factor $\sum_{m_s, m_s'} \sigma_{m_s' m_s}^{dbsq, AF \to F} \langle m_s | \{s - u_Q(s \cdot u_Q)\}_\alpha | m_s' \rangle$. We also implemented the Er(III) form factors $[F_{Er^{3+}}(Q)]_{\alpha m_j m_j'}$ as reviewed by Balcar and Lovesey in The Magnetic Neutron and Photon Scattering[7]:

$$[F_{Er^{3+}}(Q)]_{\alpha m_j m_j'} = \sum_k^{0,2,4,6} c_k(m_j, m_j', \alpha, \theta_Q, \phi_Q) \langle j_k(Q) \rangle \qquad (S10)$$

where the Q-dependence is given by the functions $\langle j_k(Q) \rangle$. The coefficients $c_k(m_j, m_j', \alpha, \theta_Q, \phi_Q)$ in Eq. S10 have an exactly computable form, which we have implemented following the angular momentum techniques reported in Balcar and Lovesey in "The Magnetic Neutron and Photon Scattering". These are expansion coefficients dependent on: (i) the m_j and m_j' quantum numbers involved in the specific transition, (ii) the Cartesian component α of the INS transition operator that is being evaluated, (iii) the polar angles θ_Q, ϕ_Q describing the orientation of the momentum transfer vector Q of modulus Q with respect to the **Er-dbsq** magnetic anisotropy axis. Thus to evaluate the powder average of the square of Eq. S10, we proceed by spherical Integration of the coefficients $c_k(m_j, m_j', \alpha, \theta_Q, \phi_Q)$, together with $F_{dbsq}(Q)$ and the associated angular factor as per Eq. S10.

The results are reported in Figure S33 (green solid line), superimposed to the experiment (red datapoints with error bars), and to the form factors that we obtain by artificially setting either $\sigma_{m_j' m_j}^{Er, AF \to F} = 0$ to mimic the form factor a pure dbsq-based transition, taking also into account the complexity of the wavefunction (blue dashed line), or $\sigma_{m_s' m_s}^{dbsq, AF \to F} = 0$ to mimic the form factor a pure Er-based transition, taking also into account the complexity of the wavefunction (orange dashed line).

It is immediately evident that while the Er-based and dbsq-based form factors (even if computed using our model of the reproduced *ab initio* wavefunctions as described in Model 2) are monotonically decaying functions of Q that are incapable of capturing the oscillatory behaviour of the observed Q-dependence. On the contrary, the full form factor based on the sum of the dbsq-based excitations (described by the density matrix $\sigma_{m'_s m_s}^{dbsq,AF \to F}$ calculated in Model 2) and Er-based $4f$ excitations (described by the density matrix $\sigma_{m'_j m_j}^{Er,AF \to F}$ calculated in Model 2), shows the appearance of an oscillatory behaviour, which cannot be understood simply in terms of the sum of Er-based and dbsq-based transitions, but is explained by the quantum coherent superposition (interference) between these excitations.

To understand this we should realise that the matrix element computed in Eq. S10 is a complex number arising from two complex contributions:

$$F_{\text{tot}}(\boldsymbol{Q}) = \tilde{F}_{\text{dbsq}}(\boldsymbol{Q}) + \tilde{F}_{\text{Er}}(\boldsymbol{Q})$$

$$(S11)$$

Where $\tilde{F}_{\text{dbsq}}(\boldsymbol{Q}) = F_{\text{dbsq}}(\boldsymbol{Q}) \sum_{m_s, m'_s} \sigma_{m'_s m_s}^{dbsq,AF \to F} \left\langle m_s \left| \{\boldsymbol{s} - \boldsymbol{u}_Q(\boldsymbol{s} \cdot \boldsymbol{u}_Q)\}_\alpha \right| m'_s \right\rangle$, and $\tilde{F}_{\text{Er}}(\boldsymbol{Q}) = \sum_{m_j, m'_j} \sigma_{m'_j m_j}^{Er,AF \to F} [F_{\text{Er}^{3+}}(\boldsymbol{Q})]_{\alpha m_j m'_j}$. Upon spherical integration of the modulus square of this complex number we will obtain:

$$|F_{\text{tot}}(Q)|^2 = \left| \tilde{F}_{\text{dbsq}}(Q) \right|^2 + \left| \tilde{F}_{\text{Er}}(Q) \right|^2 + 2\text{Re}\left(\tilde{F}_{\text{dbsq}}(Q)\tilde{F}_{Er}^*(Q) \right)$$

$$(S12)$$

Where $\left| \tilde{F}_{\text{dbsq}}(Q) \right|^2$ and $\left| \tilde{F}_{\text{Er}}(Q) \right|^2$ are associated to the dashed-line plots reported in Figure S33, while the interference term $2\text{Re}\left(\tilde{F}_{\text{dbsq}}(Q)\tilde{F}_{Er}^*(Q) \right)$ will cause the resulting form factor to

deviate from a simple average between the dbsq-based and Er-based transition, and gives rise to the oscillatory behaviour.
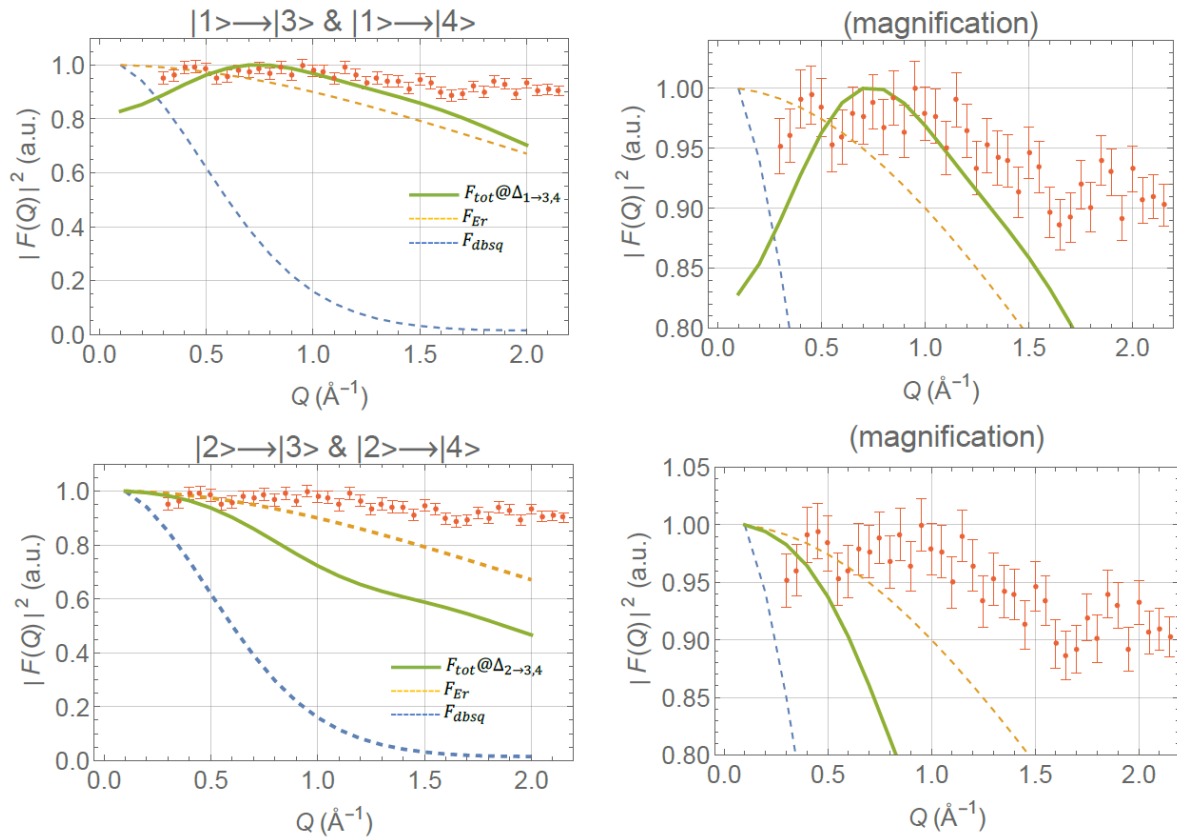

Figure S33. Calculated form factor $|F_{tot}(Q)|^2 = \left|\tilde{F}_{dbsq}(Q)\right|^2 + \left|\tilde{F}_{Er}(Q)\right|^2 + 2\mathrm{Re}\left(\tilde{F}_{dbsq}(Q)\tilde{F}_{Er}^*(Q)\right)$ estimated using Eq. S10 and Model 2 for the 1→3,4 transition (green solid line in top row panels) and 2→3,4 transition (green solid line in bottom row panels), superimposed to the experimental form factor measured for the 0.918 meV INS transition (red datapoints). The separate calculation of the Er-based transition only ($\left|\tilde{F}_{Er}(Q)\right|^2$, orange dashed line) and of the dbsq-based transition only ($\left|\tilde{F}_{dbsq}(Q)\right|^2$, blue dashed line) are also reported.

We note that while both transitions (1→3,4) and (2→3,4) display an incipient oscillatory behaviour, the form factor for the higher energy transition (1→3,4) approximates the experimental observations more closely than the transition (2→3,4).

Disagreements between calculated and observed form factors can be attributed both to the approximate nature of the CASSCF/RASSI-SO *ab initio* wavefunction, which for example, does not include dynamical correlation effects such as spin-polarization of the dbsq-radical moiety arising from $\pi-\pi^*$ excitations that could increase oscillatory behaviour for small Q values, and to the approximate nature of our own Model 2, which not only assumes that the crystal field of **Er-dbsq** is well described by that of **Er-trop**, but also represents the 4*f*-radical exchange interactions with a simplified anisotropic effective spin-Hamiltonian reproducing the lower energies of the *ab initio* energy spectrum. It should be stressed however, that even if we captured exactly the CASSCF/RASSI-SO exchange states, these would most probably still be rather approximate descriptions of the exchange and crystal field states, on account of the lack of dynamical correlation effects. Some shortcomings in the *ab initio* description are already evident from the description of the magnetic properties reported in Figures S31 and S32.

References

1   A. Caneschi, A. Dei, D. Gatteschi, L. Sorace and K. Vostrikova, *Angewandte Chemie International Edition*, 2000, **39**, 246–248.

2   T. Kanetomo and T. Ishida, *Inorg Chem*, 2014, **53**, 10794–10796.

3   M. L. Baker, T. Tanaka, R. Murakami, S. Ohira-Kawamura, K. Nakajima, T. Ishida and H. Nojiri, *Inorg Chem*, 2015, **54**, 5732–5738.

4   S. Demir, M. I. Gonzalez, L. E. Darago, W. J. Evans and J. R. Long, *Nat Commun*, 2017, **8**, 2144–2152.

5   C. A. Gould, J. Marbey, V. Vieru, D. A. Marchiori, R. David Britt, L. F. Chibotaru, S. Hill and J. R. Long, *Nat Chem*, 2021, **13**, 1001–1005.

6   N. Bajaj, N. Mavragani, A. A. Kitos, D. Chartrand, T. Maris, A. Mansikkamäki and M. Murugesu, *Hard Single-Molecule Magnet Behavior and Strong Magnetic Coupling in Radical-Bridged Ln 2 and Ln 4 Metallocenes*, .

7   N. Mavragani, A. A. Kitos, A. Mansikkamäki and M. Murugesu, *Inorg Chem Front*, 2023, **10**, 259–266.

8   P. Zhang, F. Benner, N. F. Chilton and S. Demir, *Chem*, 2022, **8**, 717–730.

9   F. Liu, L. Spree, D. S. Krylov, G. Velkos, S. M. Avdoshenko and A. A. Popov, *Acc Chem Res*, 2019, **52**, 2981–2993.

10   F. Liu, G. Velkos, D. S. Krylov, L. Spree, M. Zalibera, R. Ray, N. A. Samoylova, C.-H. Chen, M. Rosenkranz, S. Schiemenz, F. Ziegs, K. Nenkov, A. Kostanyan, T. Greber, A. U. B. Wolter, M. Richter, B. Büchner, S. M. Avdoshenko and A. A. Popov, *Nat Commun*, 2019, **10**, 571.

11   C. A. Gould, K. R. McClain, D. Reta, J. G. C. Kragskow, D. A. Marchiori, E. Lachman, E.-S. Choi, J. G. Analytis, R. D. Britt, N. F. Chilton, B. G. Harvey and J. R. Long, *Science*, 2022, **375**, 198–202.

12   S. Trofimenko, *J Am Chem Soc*, 1967, **89**, 3170–3177.

13   A. Caneschi, A. Dei, D. Gatteschi, S. Poussereau and L. Sorace, *Dalton Trans.*, 2004, **24**, 1048–1055.

14   CrysAlisPRO, Oxford Diffraction /Agilent Technologies UK Ltd, Yarnton, England.

15   G. M. Sheldrick, *Acta Crystallogr A*, 2015, **71**, 3–8.

16   G. M. Sheldrick, *Acta Crystallogr C Struct Chem*, 2015, **71**, 3–8.

17   O. V. Dolomanov, L. J. Bourhis, R. J. Gildea, J. A. K. Howard and H. Puschmann, *J Appl Crystallogr*, 2009, **42**, 339–341.

18   C. F. Macrae, I. Sovago, S. J. Cottrell, P. T. A. Galek, P. McCabe, E. Pidcock, M. Platings, G. P. Shields, J. S. Stevens, M. Towler and P. A. Wood, *J Appl Crystallogr*, 2020, **53**, 226–235.

19   S. Stoll and A. Schweiger, *Journal of Magnetic Resonance*, 2006, **178**, 42–55.

20   D. Yu, R. Mole, T. Noakes, S. Kennedy and R. Robinson, *J Physical Soc Japan*, 2013, **82**, SA027.

21   D. Yu, R. A. Mole and G. J. Kearley, *EPJ Web Conf*, 2015, **83**, 03019.

22   D. Richard, M. Ferrand and G. J. Kearley, *Journal of Neutron Research*, 1996, **4**, 33–39.

23   N. F. Chilton, R. P. Anderson, L. D. Turner, A. Soncini and K. S. Murray, *J Comput Chem*, 2013, **34**, 1164–1175.

24   Frank Jensen, *Introduction to Computational Chemistry*, John Wiley & Sons, Ltd., Chichester West Sussex, UK, 3rd Editio., 2017.

25   P. Å. Malmqvist, B. O. Roos and B. Schimmelpfennig, *Chem Phys Lett*, 2002, **357**, 230–240.

26   I. Fdez. Galván, M. Vacher, A. Alavi, C. Angeli, F. Aquilante, J. Autschbach, J. J. Bao, S. I. Bokarev, N. A. Bogdanov, R. K. Carlson, L. F. Chibotaru, J. Creutzberg, N.

Dattani, M. G. Delcey, S. S. Dong, A. Dreuw, L. Freitag, L. M. Frutos, L. Gagliardi, F. Gendron, A. Giussani, L. González, G. Grell, M. Guo, C. E. Hoyer, M. Johansson, S. Keller, S. Knecht, G. Kovačević, E. Källman, G. Li Manni, M. Lundberg, Y. Ma, S. Mai, J. P. Malhado, P. Å. Malmqvist, P. Marquetand, S. A. Mewes, J. Norell, M. Olivucci, M. Oppel, Q. M. Phung, K. Pierloot, F. Plasser, M. Reiher, A. M. Sand, I. Schapiro, P. Sharma, C. J. Stein, L. K. Sørensen, D. G. Truhlar, M. Ugandi, L. Ungur, A. Valentini, S. Vancoillie, V. Veryazov, O. Weser, T. A. Wesołowski, P.-O. Widmark, S. Wouters, A. Zech, J. P. Zobel and R. Lindh, *J Chem Theory Comput*, 2019, **15**, 5925–5964.

27   F. Aquilante, J. Autschbach, A. Baiardi, S. Battaglia, V. A. Borin, L. F. Chibotaru, I. Conti, L. De Vico, M. Delcey, I. Fdez. Galván, N. Ferré, L. Freitag, M. Garavelli, X. Gong, S. Knecht, E. D. Larsson, R. Lindh, M. Lundberg, P. Å. Malmqvist, A. Nenov, J. Norell, M. Odelius, M. Olivucci, T. B. Pedersen, L. Pedraza-González, Q. M. Phung, K. Pierloot, M. Reiher, I. Schapiro, J. Segarra-Martí, F. Segatta, L. Seijo, S. Sen, D.-C. Sergentu, C. J. Stein, L. Ungur, M. Vacher, A. Valentini and V. Veryazov, *J Chem Phys*, 2020, **152**, 214117.

28   B. O. Roos, R. Lindh, P.-Å. Malmqvist, V. Veryazov, P.-O. Widmark and A. C. Borin, *J Phys Chem A*, 2008, **112**, 11431–11435.

29   M. Reiher and A. Wolf, *Relativistic Quantum Chemistry: The Fundamental Theory of Molecular Science*, John Wiley & Sons, Ltd., Chichester West Sussex, UK, 2nd Editio., 2014.

30   L. F. Chibotaru and L. Ungur, *J Chem Phys*, 2012, **137**, 064112.

31   F. Aquilante, T. B. Pedersen and R. Lindh, *J Chem Phys*, 2007, **126**, 194106.

32   J. Rodríguez-Carvajal, *Physica B Condens Matter*, 1993, **192**, 55–69.

33   I. S. Anderson, P. J. Brown, J. M. Carpenter, G. Lander, R. Pynn, J. M. Rowe, O. Schärpf, V. F. Sears and B. T. M. Willis, in *International Tables for Crystallography*, International Union of Crystallography, Chester, England, 2006, vol. C, pp. 430–487.

34   H. U. Güdel, A. Furrer, H. Blank and H. Blankic, *Inorg Chem*, 1990, **29**, 4081–4084.

35   G. K. Gransbury, M.-E. Boulon, R. A. Mole, R. W. Gable, B. Moubaraki, K. S. Murray, L. Sorace, A. Soncini and C. Boskovic, *Chem Sci*, 2019, **10**, 8855–8871.

36   M. J. Giansiracusa, E. Moreno-Pineda, R. Hussain, R. Marx, M. Martínez Prada, P. Neugebauer, S. Al-Badran, D. Collison, F. Tuna, J. van Slageren, S. Carretta, T. Guidi, E. J. L. McInnes, R. E. P. Winpenny and N. F. Chilton, *J Am Chem Soc*, 2018, **140**, 2504–2513.

37   P. Zhang, M. Perfetti, M. Kern, P. P. Hallmen, L. Ungur, S. Lenz, M. R. Ringenberg, W. Frey, H. Stoll, G. Rauhut and J. van Slageren, *Chem Sci*, 2018, **9**, 1221–1230.

38   W. R. Reed, M. A. Dunstan, R. W. Gable, W. Phonsri, K. S. Murray, R. A. Mole and C. Boskovic, *Dalton Transactions*, 2019, **48**, 15635–15645.